Stratospheric Response to the 11-Yr Solar Cycle: Breaking Planetary Waves, Internal Reflection, and Resonance

HUA LU

British Antarctic Survey, Cambridge, United Kingdom

LESLEY J. GRAY

Clarendon Laboratory, Department of Physics, Oxford University, Oxford, and National Centre for Atmospheric Science, Natural Environment Research Council, Leeds, United Kingdom

IAN P. WHITE

British Antarctic Survey, Cambridge, United Kingdom, and Institute of Earth Sciences, Hebrew University of Jerusalem, Israel

THOMAS J. BRACEGIRDLE

British Antarctic Survey, Cambridge, United Kingdom

(Manuscript received 13 January 2017, in final form 17 May 2017)

ABSTRACT

Breaking planetary waves (BPWs) affect stratospheric dynamics by reshaping the waveguides, causing internal wave reflection, and preconditioning sudden stratospheric warmings. This study examines observed changes in BPWs during the northern winter resulting from enhanced solar forcing and the consequent effect on the seasonal development of the polar vortex. During the period 1979–2014, solar-induced changes in BPWs were first observed in the uppermost stratosphere. High solar forcing was marked by sharpening of the potential vorticity (PV) gradient at 30°–45°N, enhanced wave absorption at high latitudes, and a reduced PV gradient between these regions. These anomalies instigated an equatorward shift of the upper-stratospheric waveguide and enhanced downward wave reflection at high latitudes. The equatorward refraction of reflected waves from the polar upper stratosphere then led to enhanced wave absorption at 35°–45°N and 7–20 hPa, indicative of a widening of the midstratospheric surf zone. The stratospheric waveguide was thus constricted at about 45°–60°N and 5–10 hPa in early boreal winter; reduced upward wave propagation through this region resulted in a stronger upper-stratospheric westerly jet. From January, the regions with enhanced BPWs acted as ''barriers'' for subsequent upward and equatorward wave propagation. As the waves were trapped within the stratosphere, anomalies of zonal wavenumbers 2 and 3 were reflected poleward from the stratospheric surf zone. Resonant excitation of some of these reflected waves resulted in rapid growth of wave disturbances and a more disturbed polar vortex in late winter. These results provide a process-oriented explanation for the observed solar cycle signal. They also highlight the importance of nonlinearity in the processes that drive the stratospheric response to external forcing.

1. Introduction

Over an 11-yr solar cycle, the incoming total solar irradiance changes by less than 0.1% (Lean 2000), but in the UV the variations reach several percent (Lean 2000). The formation of stratospheric ozone involves chemical reactions of oxygen atoms and molecules and their interaction with solar ultraviolet (UV) irradiance. The thermal condition and dynamical structure of the stratosphere depends critically on the distribution of ozone (Brasseur and Solomon 2005). Studies show that there is a 2%–4% increase in annual-mean ozone in the low-latitude mid-to-upper stratosphere and an approximate 1-K increase in annual mean temperature in the equatorial upper stratosphere and lower mesosphere during high solar activity years compared to solar minimum conditions (Haigh 2003; Remsberg 2014; Mitchell et al. 2015a; Hood et al. 2015; Dhomse et al. 2016).

Corresponding author: Hua Lu, hlu@bas.ac.uk

DOI: 10.1175/JCLI-D-17-0023.1

During the last three decades, major research efforts have investigated the extent to which atmospheric circulation may respond to this localized radiative forcing (Kodera and Kuroda 2002; Haigh 2003; Gray et al. 2010; Ineson et al. 2011; Cnossen et al. 2011; Hitchcock and Haynes 2016). However, an accurate, process-based quantification remains elusive as a result of a large spread in the solar UV and ozone measurements (Ermolli et al. 2013; Hood et al. 2015; Ball et al. 2016), uncertainties among reanalysis datasets (Dee et al. 2011; Lu et al. 2015; Mitchell et al. 2015a; Martineau et al. 2016), and model biases (Mitchell et al. 2015b; Dhomse et al. 2016).

It has been widely accepted that the atmospheric response to the initially small-magnitude solar radiative forcing must involve amplification via nonlinear processes (Gray et al. 2010). One classic mechanism involves the dynamical interaction between upward-propagating planetary-scale Rossby waves (planetary waves hereafter) and the background westerly flow in the winter stratosphere. When a critical layer in a vertical shear flow is encountered by upward-propagating planetary waves, where the phase speed of the wave matches that of the background flow, strong mixing taking place below the critical layer and leads to deceleration of the zonal-mean westerly winds (Matsuno 1971). Subsequent waves are then absorbed below the decelerating region. Wave breaking continues to occur below the critical line, resulting in the downward movement of easterly anomalies. This mechanism appears to operate during solar minimum winters when the upper-stratospheric subtropical westerlies are relatively weak. Conversely, during high solar activity years the enhanced solar UV irradiance results in a steeper meridional temperature gradient near the subtropical upper stratosphere–lower mesosphere in the winter hemisphere. In accordance with thermal wind balance and linear wave theory, a steeper meridional temperature gradient gives rise to stronger westerly winds, which may cause poleward wave refraction (Charney and Drazin 1961). Wave refraction away from the westerly polar vortex leads to a reduction of net wave drag on the mean flow. A positive feedback between the mean flow and waves results in a further strengthening of the polar vortex and a weakened meridional overturning circulation (Kodera and Kuroda 2002). Thus, enhanced solar UV forcing would result in a poleward and downward movement of westerly wind anomalies.

Recent studies based on reanalysis datasets have however shown that a continuous downward movement of westerly zonal-mean anomalies cannot be detected statistically during either the Northern or Southern Hemisphere winters (Mitchell et al. 2015a,b; Yamashita et al. 2015; Lu et al. 2011, 2017). Instead, these studies show that westerly wind anomalies appear to be confined to the subtropical upper stratosphere in early winter (November–December), and in late winter (February) a downward movement of easterly anomalies is observed, which originate from the upper stratosphere. The latter has been interpreted as the delayed occurrence of sudden stratospheric warmings (SSWs) under solar maximum conditions (Gray et al. 2004; Cnossen et al. 2011), with SSWs occurring in early to midwinter under solar minimum conditions and in late winter under solar maximum conditions. A similar sign reversal of early- and late-winter circulation anomalies has also been reported in model simulations (e.g., Ineson et al. 2011; Chiodo et al. 2012; Marchand et al. 2012). However, if the poleward and downward movement of westerly anomalies in early winter cannot be observed (Lu et al. 2017; Mitchell et al. 2015a), it is possible that the classic mechanism of wave refraction may not be the dominant mechanism, and other reasons must be sought to explain the sign reversal of the solar signal between early and late winter.

Several nonlinear processes may alter the stratospheric waveguide and the seasonal development of the polar vortex. Breaking planetary wave (BPW) events that involve an irreversible mixing of potential vorticity (PV) play a crucial role in shaping winter stratospheric dynamics and preconditioning SSWs (McIntyre 1982; Albers and Birner 2014). A BPW event is manifested by filaments of high-PV air being drawn out from the edge of the polar vortex while strips of low-PV air spiral from the subtropics or from the high latitudes (McIntyre and Palmer 1983; Waugh and Dritschel 1999). The PV mixing in the surf zone and PV sharpening near the polar vortex edge modify the stratospheric waveguide and subsequent wave propagation and absorption (Plumb 2010). Idealized studies also show that shear instability may lead to BPWs or enhanced filamentation (Dritschel 1986). Furthermore, gravity waves are able to impose wave drag on the mean flow in the upper stratosphere and the lower mesosphere (Andrews et al. 1987) and, in particular, have been shown to precondition SSWs in a similar way to BPWs (Albers and Birner 2014).

The intensity and characteristics of BPWs are intimately related to the absorbing/reflecting properties of critical layers. While the general evolution of a critical layer involves a damped oscillation between wave absorption, reflection, and overreflection, the details are sensitive to many factors, especially dissipation and instability (Stewartson 1977; Killworth and McIntyre 1985).

The internally generated and/or reflected transient waves may lead to important dynamical consequences

elsewhere (Walker and Magnusdottir 2003; Abatzoglou and Magnusdottir 2006), especially when these waves are trapped in a resonant cavity, in which case a rapid increase in wave amplitudes can lead to a sudden disruption of the polar vortex (Tung 1979; Tung and Lindzen 1979a,b). In extreme cases, they are able to produce an SSW (Esler and Matthewman 2011). Furthermore, nonlinear wave–wave interaction acts to tune and excite wave growth when a system is initially off-resonant (Plumb 1981). Internal wave reflection is a necessary condition for such a ''self tuning'' process to take place. To date, the extent to which these processes may be affected by the variation of solar UV–ozone photochemistry over the 11-yr cycle remains largely unexplored.

A recent study showed that downward wave reflection was significantly enhanced in the northern high-latitude stratosphere during high solar activity winters (Lu et al. 2017). The effect involved enhanced barotropic instability near the polar night jet at approximately 45°–60°N and 1–3 hPa and enhanced BPWs in the high-latitude upper stratosphere. The enhanced wave breaking led to a reflecting surface forming in the polar upper stratosphere, which instigated the downward wave reflection during November–January. It is noted that the solar-induced downward wave reflection occurred with a stable polar vortex in the mid- and lower stratosphere, differing from those following SSWs.

The present work examines the extent to which these upper-level BPWs may play a role in causing changes in planetary wave propagation and breaking in the mid- and lower stratosphere. We show how the observed sign reversal of the circulation anomalies between early and late winter in the northern stratosphere may be linked to these BPWs. The effect is further examined in relation to changes in stratospheric waveguides, internal wave reflection, and resonance. Finally, a mechanistic view is provided to explain the chain of events.

2. Data and methods

a. Data and statistical diagnostics

This study uses ERA-Interim for 1979–2014 with 37 levels extending up to 1 hPa (Dee et al. 2011). This dataset is chosen mainly because it has a good representation of the temperature and circulation in the upper stratosphere, where the direct radiative effect of solar UV via photochemical processes takes place (Hood et al. 2015). We are fully aware of the common problem among all the reanalysis datasets that the ozone and temperature profile in the upper stratosphere may not be well constrained by observations. This problem deteriorates back in time and becomes severe in the presatellite era (i.e., before 1979) when there were little real measurements above 10 hPa. To avoid the bias and contamination from the presatellite era in the upper-stratospheric reanalysis, we decided not to include data before 1979. In addition, three other reanalysis datasets including JRA-55, MERRA, and NCEP CFSR covering the period of 1979–2012 are used to check the robustness of the Eliassen–Palm (E-P) flux analysis in the upper stratosphere. Details regarding the type of model, horizontal and vertical resolutions, and the height of the upper lid of each of the reanalysis datasets employed can be found in Table 1 of Mitchell et al. (2015a).

The daily Mg II core-to-wing index (Viereck and Puga 1999) is used to represent solar UV variation for this same period. These data were derived from the *Nimbus-7* solar backscatter UV (SBUV) spectrometer and calibrated using the Solar Stellar Irradiance Comparison Experiment (SOLSTICE) and the high spectral resolution Global Ozone Monitoring Experiment (GOME) measurements (deToma et al. 1997). Following Chiodo et al. (2014), we excluded three winters (i.e., 1982/83, 1991/92, and 1992/93) to avoid aliasing of the volcanic signal. Our analysis included the winters affected by the major ENSO events since we found no clear evidence to suggest that the solar signal was sensitive to those ENSO events. We are also aware that the solar signal could be further modulated by the quasi-biennial oscillation (QBO) (e.g., Labitzke 1987; Lu et al. 2009) and solar energetic particle precipitation (e.g., Seppälä et al. 2013). Limited by the sample size, these effects were not considered here. As such, our seasonal averages were based on 11 high solar (HS) activity winters (1979/80, 1980/81, 1981/82, 1988/89, 1989/90, 1990/91, 1999/2000, 2000/01, 2001/02, 2002/03, and 2003/04) and 16 low solar (LS) activity winters (1984/85, 1985/86, 1986/87, 1987/88, 1993/94, 1994/95, 1995/96, 1996/97, 1997/98, 2004/05, 2005/06, 2006/07, 2007/08, 2008/09, 2009/10, and 2010/11), with 6 solar neutral years (i.e., 1983/84, 1998/99, 2003/04, 2011/12, 2012/13,and 2013/14) excluded from the analysis. The list may change slightly as the seasonal-mean changes accordingly when running averages are performed. A time series plot that shows how the HS and LS subgroups are defined based on monthly mean Mg II index (black line) can be found in Fig. 1 of Lu et al. (2017). Statistical significance of the composite differences between HS and LS subgroups (HS − LS) was estimated by the two-sided Student's t test.

To examine the temporal evolution of a circulation field and its different behavior under HS and LS conditions, running composite analyses with a one-day time step and a centered average window of 31 days is performed for HS and LS subgroups, respectively. The

average window is used mainly to reduce the contamination from short-term internal variability. The 3-month-averaged Mg II indices for the months preceding the last day of the average window were used as the forcing variable to divide the data into the HS and LS subgroups, depending on whether the averaged Mg II indices were greater or smaller than the seasonal mean ±0.002. The confidence intervals of the running averages are calculated by $\mu \pm z\sigma/\sqrt{n}$, where μ is the sample mean, σ is standard deviation, and n is the number of samples. We set $z = 1.645$ for the 90% confidence level.

b. The E-P flux divergence

The E-P flux divergence $\nabla \cdot \mathbf{F}$ is used to measure the wave driving of the zonal-mean circulation (Andrews et al. 1987). In spherical log-pressure coordinates this takes the following form:

$$\nabla \cdot \mathrm{F} = \frac{1}{a\cos\phi}[F^{(\phi)}\cos\phi]_{\phi} + F^{(z)}, \tag{1}$$

where the meridional and vertical E-P fluxes $F^{(\phi)}$ and $F^{(z)}$ are

$$F^{(\phi)} = \rho_0 a\cos\phi\left(\frac{\overline{v'\theta'}}{\theta_z}\overline{u}_z - \overline{v'u'}\right) \quad \text{and}$$

$$F^{(z)} = \rho_0 a\cos\phi\left\{\left[f - \frac{1}{a\cos\phi}(\overline{u}\cos\phi)_{\phi}\right]\frac{\overline{v'\theta'}}{\theta_z} - \overline{w'u'}\right\}, \tag{2}$$

where a is the mean radius of Earth, f is the Coriolis parameter, z is log-pressure height, ϕ is latitude, θ is potential temperature, and u, v, and w are zonal, meridional, and vertical velocities, respectively. The overbar, prime, and subscript denote zonal average, departures from zonal average, and derivative, respectively.

The calculations of E-P fluxes and divergence were carried out for the total wave forcing and further separated into stationary and planetary contributions (i.e., zonal wavenumbers 1, 2, and 3 only). To calculate the stationary wave contribution, the atmospheric variables were first averaged over a season at each grid point. To calculate the contributions from planetary waves, a fast Fourier transform filter was applied longitudinally to select the required wavenumbers.

To help visualize the wave propagation directions, the E-P fluxes were scaled in the form of $\tilde{\mathbf{F}} = [\tilde{F}^{(\phi)}, \tilde{F}^{(z)}] = (p_s/p)^{0.85}[F^{(\phi)}/(a\pi), F^{(z)}/(3\times10^5)]$ (Edmon et al. 1980). An additional factor of 10 was applied to the solar cycle differences (i.e., the difference fields related to HS and LS subgroups). The divergence was estimated as $\nabla \cdot \tilde{\mathbf{F}} = \nabla \cdot \mathbf{F}/\rho_0 a\cos\phi$ (which has the units of $\mathrm{m\,s^{-1}\,day^{-1}}$). Unlike the E-P fluxes, no scaling is applied to $\nabla \cdot \tilde{\mathbf{F}}$ for climatology or the solar differences.

c. Waveguide diagnostics

The refractive index is a measure of planetary wave waveguide (Matsuno 1970). In spherical coordinates, it takes the following form:

$$n_k^2 = \frac{\overline{q}_{\phi}}{a(\overline{u}-c)} - \left(\frac{k}{a\cos\phi}\right)^2 - \left(\frac{f}{2NH}\right)^2, \tag{3}$$

where c is the phase speed of the waves, k is the zonal wavenumber, H is the mean scale height (=7 km), N is the buoyancy frequency, and $\overline{q}_{\phi}$ is the meridional gradient of the zonally averaged potential vorticity (PV gradient hereafter). The PV gradient is calculated as

$$\overline{q}_{\phi} = 2\Omega\cos\phi - \left[\frac{(\overline{u}\cos\phi)_{\phi}}{a\cos\phi}\right]_{\phi} + \frac{af^2}{N^2}\left(\frac{\overline{u}_z}{H} - \overline{u}_{zz}\right), \tag{4}$$

where Ω is Earth's angular velocity and other symbols are the same as in section 2b.

Large positive values of $\overline{q}_{\phi}$ and n_k^2 support wave propagation while flow vacillation and wave breaking occur when both $\overline{q}_{\phi}$ and n_k^2 are small or negative (Matsuno 1970; Holton and Mass 1976). Small and negative $\overline{q}_{\phi}$ also suggest barotropic instability (Kuo 1949). The value of n_k^2 would become infinitely large near a critical layer (i.e., $\overline{u} - c = 0$), where BPWs and reflection occur. For quasi-stationary waves, the critical layer reduces to the zero-wind line (i.e., $\overline{u} = 0$), which is often found in the subtropics. While small-amplitude waves tend to be absorbed at the critical line, an increase in wave amplitude may lead to enhanced BPWs and nonlinear reflection (Killworth and McIntyre 1985; Walker and Magnusdottir 2003). The subtropical zero-wind line acts as an absorber for incident planetary waves from the midlatitudes if there are no BPWs on its poleward flank. Enhanced BPWs in the stratospheric surf zone act as a ''barrier'' for equatorward wave propagation, resulting in reduced wave absorption by the subtropical zero-wind line and enhanced poleward wave reflection (Plumb 2010).

Following Matsuno (1970), the refractive index for stationary waves is multiplied by a^2, where a is Earth's radius. To avoid floating errors and the excessively large spread of $a^2 n_k^2$ due to small values of $\overline{u}$, the area-averaged refractive index is calculated by removing those $a^2 n_k^2$ values when $|\overline{u}| \le 0.1\ \mathrm{m\,s^{-1}}$, where $\overline{u}$ is the

grid-based zonal-mean zonal wind over a predefined temporal period (i.e., 31-day running window).

d. Diagnostics for BPWs

BPWs are diagnosed by examining changes in the PV gradient and their favored location as well as through their unique E-P structure and relationship with the polar vortex. BPWs should be marked by enhanced PV gradients near the westerly jet axis and reduced PV gradients in the surf zone and at high latitudes. The effect must be accompanied by E-P flux divergence away from the edge of the polar vortex and convergence in the stratospheric surf zone (McIntyre and Palmer 1983). Because of the rearrangement of PV in the meridional direction, the E-P flux vectors should also be oriented in the horizontal direction rather than vertically (Esler and Matthewman 2011). These features differ distinctly from the classic mechanism that involves upward-propagating planetary waves encountering a critical layer in a vertical shear flow (Matsuno 1971; Kodera and Kuroda 2002).

e. Diagnostics for wave reflection and resonance

Forced planetary waves propagating upward from the troposphere are characterized by positive values of the momentum flux $\overline{u'v'}$ and the northward heat flux $\overline{v'T'}$, while negative $\overline{u'v'}$ and $\overline{v'T'}$ indicate internal wave reflection. Because reflection events are often episodic, their effects tend to be smeared out in seasonal averages. Here, internal wave reflection is detected using daily $\overline{u'v'}$ and $\overline{v'T'}$ following Dunn-Sigouin and Shaw (2015). Wave reflection anomalies were identified statistically by a significant increase in value and the frequent occurrence of negative daily $\overline{u'v'}$ and/or $\overline{v'T'}$. In addition, when the waves are resonantly excited, we would also expect the seasonal averages of negative daily $\overline{u'v'}$ and/or $\overline{v'T'}$ to be sufficiently larger than their climatology. The momentum and heat fluxes are used instead of the E-P fluxes $F^{(\phi)}$ and $F^{(z)}$ because they do not involve static stability θ_z, which was found to introduce relatively large biases in the upper stratosphere during data assimilation (Lu et al. 2015).

The space–time cross-spectral decomposition technique of Hayashi (1971) is applied to the daily geopotential height data to diagnose resonant growth of transient waves. The method expresses the amplitude of wave disturbance in geopotential height as a function of longitude and time. It decomposes the wave power (which has the units of m^2) further into westward and eastward propagation components based on Fourier expansion. To do this, it assumes that the standing waves correspond to the part of the spectrum that consists of coherent eastward- and westward-moving components of equal amplitude. The incoherent part of the spectrum represents traveling waves. This technique allows us to detect significant increases in wave amplitude associating with certain wavenumbers and frequencies. The detailed description of the method can be found in Hayashi (1971) while a recent application can be found in Lu et al. (2012).

3. Results

a. The reversal of the solar signal

Figure 1 shows the November–December and February–March mean climatological zonal-mean temperatures and zonal winds and their corresponding solar composite differences (HS − LS). Similar but weaker signals can be obtained based on October–December and January–March mean (not shown). The climatology shows the expected profile with a colder and stronger upper-stratospheric westerly jet in early winter (i.e., November–December), which becomes significantly weaker and warmer by late winter (i.e., February–March). The warm anomalies (~1.5 K) in the equatorial upper stratosphere (0°–20°N, 1–3 hPa) are common to both early and late winter (Figs. 1c,d). This effect is stronger and extends lower into the subtropical mid-stratosphere in early winter. There is a small region with negative temperature anomalies at 45°–60°N and 2–3 hPa (Fig. 1c), where enhanced sign reversal of the PV gradient has been found in the same region (see Fig. 7 of Lu et al. 2017). These temperature anomalies are indicative of a dynamical response to solar UV variability over the 11-yr solar cycle. As the poleward refracted waves from the upper-stratospheric subtropical jet region interact with the polar night jet, enhanced BPWs lead to localized barotropic instability as shown by Lu et al. (2017). In February–March, the extratropical stratospheric response is marked by warmer anomalies (~5 K) at 60°–90°N, 10–30 hPa and easterly anomalies at 55°–80°N and 1–5 hPa. This indicates a sign reversal of the solar signal between early and late winter, with a stronger, colder vortex under HS in early winter and a weaker, warmer vortex in late winter, as reported by earlier studies (Gray et al. 2004; Ineson et al. 2011; Mitchell et al. 2015a; Lu et al. 2017).

The solar signal in zonal-mean winds $\overline{u}$ are consistent with the temperature anomalies. Again, the wind anomalies are confined mostly to the upper-to-middle stratosphere. Although a downward extension of the westerly anomalies is present in early winter, they are not statistically significant at the $p = 0.05$ level (Figs. 1e,f). This is in agreement with previous studies including those based on multiple reanalysis datasets. Detailed

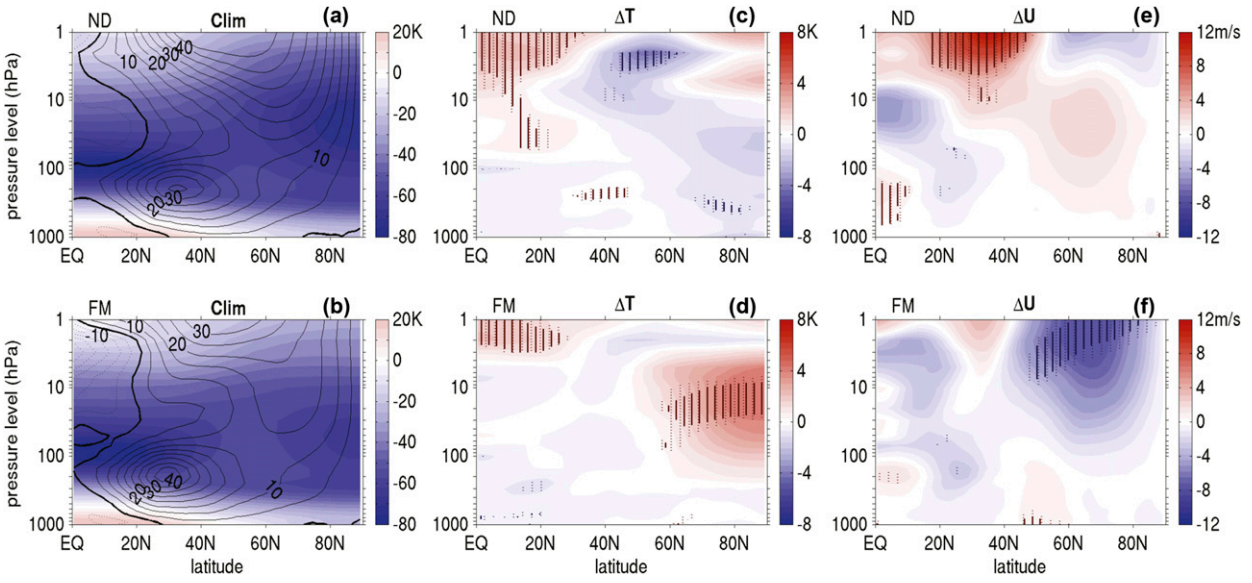

FIG. 1. Climatological zonal-mean temperature (shaded) and zonal wind (contours) for (a) November–December and (b) February–March averages. The subtropical zero-wind line is shown as the thick black line. Solar composite differences (HS − LS) for (c),(d) temperatures and (e),(f) zonal-mean zonal winds. The vertical dotted and solid lines in (c)–(f) indicate p value ≤ 0.1 and 0.05, respectively, calculated using the two-sided Student's t test.

examination of the seasonal development of solar-induced wind and temperature anomalies can be found in Mitchell et al. (2015a) and Lu et al. (2017).

Figures 2a,b show the climatology of the total E-P fluxes $\tilde{\mathbf{F}}_{\text{total}} = [\tilde{F}^{(\phi)}_{\text{total}}, \tilde{F}^{(z)}_{\text{total}}]$ (arrows) and the associated E-P flux divergence $\nabla \cdot \tilde{\mathbf{F}}_{\text{total}}$ (contours) for early winter (October–December) and late winter (January–March). Figures 2c,d show the corresponding solar composite differences. The 3-month averages are used here because the wave fields are noisier than those of wind and temperature. Also, according to the classic mechanism, we would expect the wave anomalies to lead the circulation anomalies, at least in the regions away from the subtropical upper stratosphere where the direct solar UV radiative forcing takes place. Regions with significant wave anomalies but without significant changes in the zonal-mean circulation would indicate that different mechanisms are likely to be at work.

As expected, in both early and late winter, the climatology of the NH winter wave activity is marked by upward- and equatorward-pointing E-P flux vectors with predominantly negative divergence near the regions with strong westerly winds. In early winter, solar-induced changes in E-P fluxes and divergence are marked by poleward- and downward-pointing E-P flux anomalies in the extratropical upper stratosphere, accompanied by negative $\nabla \cdot \tilde{\mathbf{F}}_{\text{total}}$ anomalies at 2–3 hPa and positive $\nabla \cdot \tilde{\mathbf{F}}_{\text{total}}$ anomalies at 3–10 hPa. While the upper-layer negative $\nabla \cdot \tilde{\mathbf{F}}_{\text{total}}$ anomalies are confined to the high latitudes, the lower-layer positive $\nabla \cdot \tilde{\mathbf{F}}_{\text{total}}$ anomalies extend from the subtropics to high latitudes. The lower-layer positive $\nabla \cdot \tilde{\mathbf{F}}_{\text{total}}$ anomalies indicate enhanced wave refraction away from the subtropical westerly jet under HS, according to the classic mechanism of Kodera and Kuroda (2002). The negative $\nabla \cdot \tilde{\mathbf{F}}_{\text{total}}$ anomalies above indicate enhanced wave breaking. The downward-pointing E-P flux anomalies in the high-latitude mid- and lower stratosphere are indicative of reduced upward wave propagation and/or enhanced downward wave reflection (Lu et al. 2017). These wave forcing anomalies would lead to reduced wave forcing on the upper-stratospheric westerly jet and thus a stronger westerly jet in the upper stratosphere. This is consistent with Figs. 1c,e. The solar signal in late winter is marked by upward- and poleward-pointing E-P flux anomalies in the extratropical stratosphere with negative $\nabla \cdot \tilde{\mathbf{F}}_{\text{total}}$ anomalies at 30°–60°N and 1–5 hPa, consistent with a warmer, more disturbed upper-level westerly jet (Figs. 1d,f). It is noted that the upward-pointing E-P flux anomalies appear to be confined to the stratosphere. Very similar results can be found for stationary waves (not shown).

Figure 3 shows the seasonal progression of the solar signal in stationary planetary waves (i.e., zonal wavenumbers 1–3). The climatological behavior of the stationary planetary E-P fluxes and divergence $\nabla \cdot \tilde{\mathbf{F}}_{\text{strat}}$ are very similar to those in Fig. 2, except for smaller magnitudes. The seasonal development of solar-cycle-induced

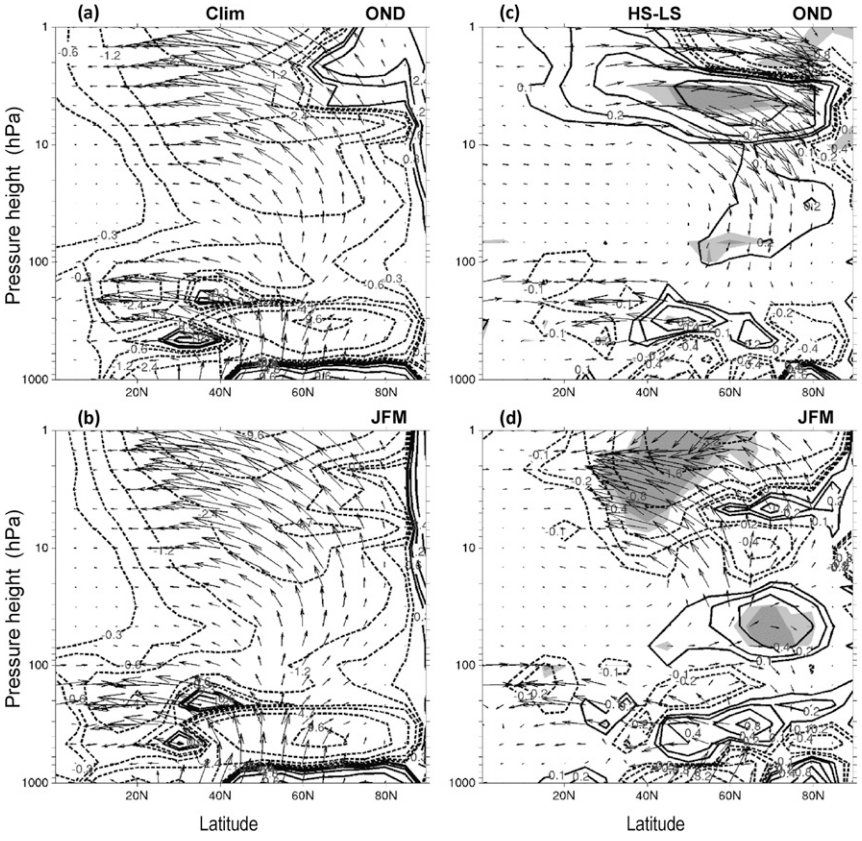

FIG. 2. The (a) October–December and (b) January–March climatological-mean E-P fluxes (arrows) and E-P flux divergence (contours) in latitude–pressure height cross section of 0°–90°N and 1000–1 hPa. (c),(d) As in (a),(b), but for their corresponding solar composite differences (HS − LS). Note that the E-P fluxes are scaled and the difference fields were multiplied further by a factor of 10. See section 2b for more detail regarding the scaling. Solid and dashed contours are positive and negative divergence at the intervals of ±0.3, ±0.6, ±1.2, ±2.4, … m s^{-1} day^{-1} for (a),(b)and ±0.1, ±0.2, ±0.4, ±0.8, … m s^{-1} day^{-1} for (c),(d). The light and dark gray-shaded areas represent p values ≤ 0.1 and 0.05, respectively.

$\nabla \cdot \tilde{\mathbf{F}}_{\text{strat}}$ anomalies can be described as follows. Positive $\nabla \cdot \tilde{\mathbf{F}}_{\text{strat}}$ anomalies first appear at 30°–40°N and 3–5 hPa in October–November and then expand poleward toward the polar night jet in November–December. They then move downward into the lower stratosphere in December–January. These positive $\nabla \cdot \tilde{\mathbf{F}}_{\text{strat}}$ anomalies are associated with E-P flux vectors diverging away from the polar vortex edge. Negative $\nabla \cdot \tilde{\mathbf{F}}_{\text{strat}}$ anomalies first appear in the polar stratosphere in October–December. They are associated with downward- and then equatorward-pointing E-P flux anomalies. Negative $\nabla \cdot \tilde{\mathbf{F}}_{\text{strat}}$ anomalies subsequently appear in the stratospheric surf zone at 35°–45°N and 2–20 hPa in December–January. These convergent anomalies intensify and expand upward in January–February. They are associated with E-P flux anomalies emitted out from the polar vortex edge, indicating an equatorward expansion of the surf zone due to enhanced BPWs.

Not shown here, we also find that solar-induced changes in transient wave E-P fluxes and divergence in early to midwinter are predominantly featured by the meridional E-P flux anomalies. In early winter, the transient wave anomalies account for part of the enhanced poleward wave reflection in the upper stratosphere and equatorward wave propagation in the midstratosphere. In midwinter, poleward-pointing transient wave E-P flux anomalies emerge from the region with enhanced BPWs, indicating enhanced poleward reflection. In late winter, transient waves account for the major part of the vertical and upward E-P flux anomalies along the poleward flank of the polar vortex. Thus, solar-induced anomalies of the E-P flux divergence $\nabla \cdot \tilde{\mathbf{F}}$ all exhibit a sign reversal between early and late winter, whether or not they are dominated by meridional or vertically E-P fluxes.

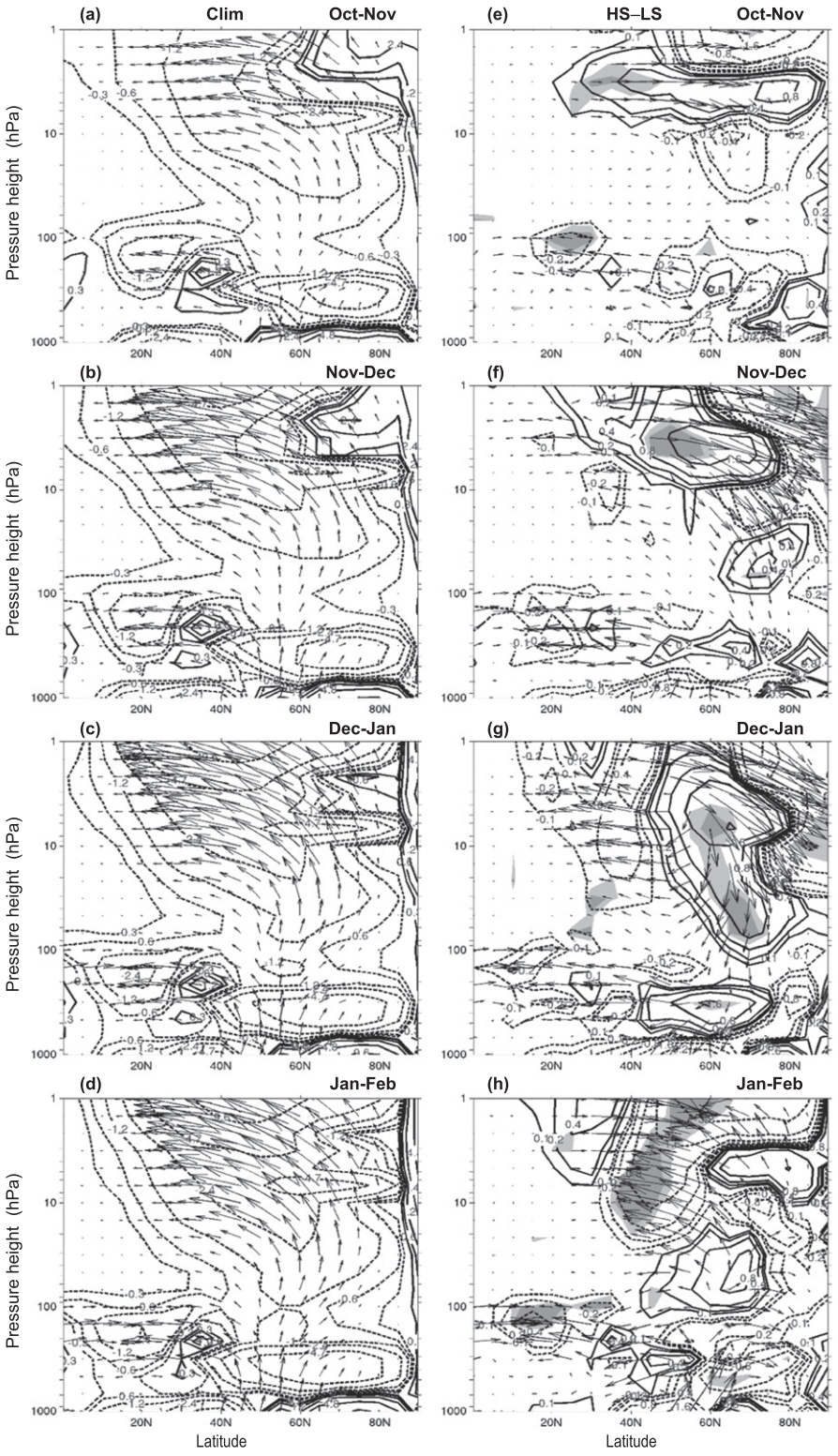

FIG. 3. (a)–(d) As in Fig. 2a,b, but for 2-month running averages of stationary planetary waves averaged from October–November to January–February. (e)–(h) Corresponding solar composite differences. The arrows, contours, shading, and scaling applied to the E-P fluxes and anomalies are as in Fig. 2.

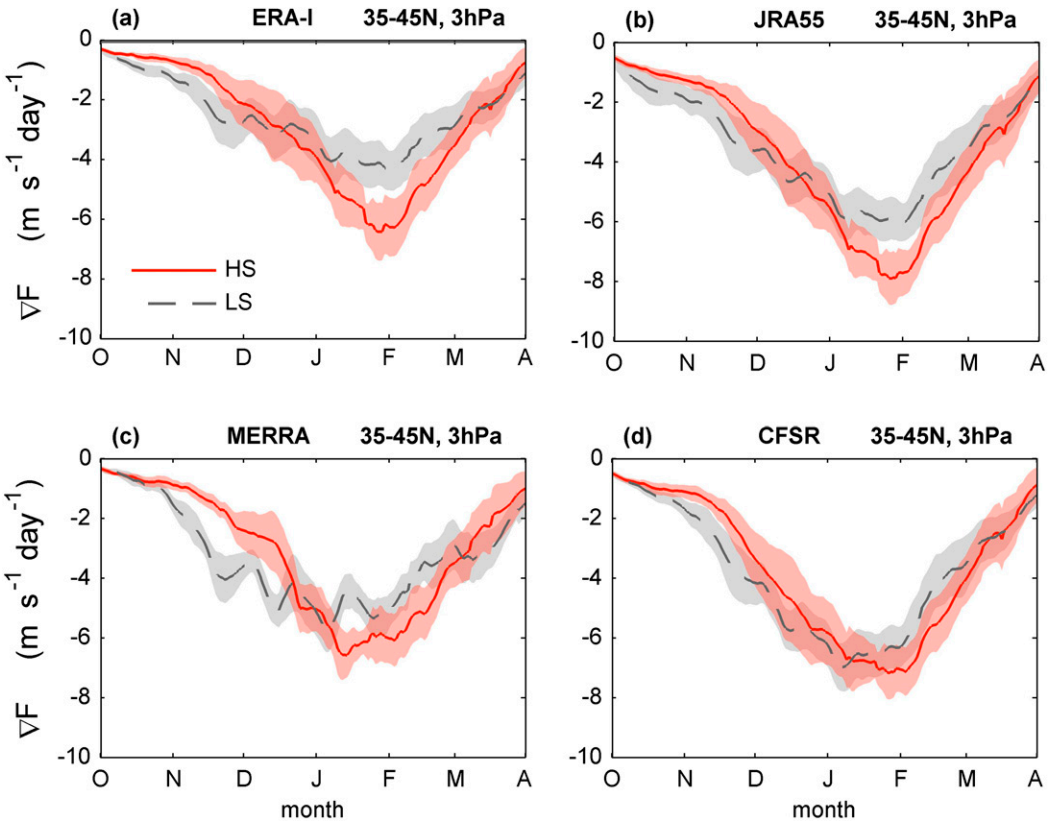

FIG. 4. The 31-day running averages of the planetary wave (i.e., zonal wavenumbers 1–3) E-P flux divergence $\nabla \cdot \tilde{\mathbf{F}}$ at 35°–45°N and 3 hPa estimated from four major modern reanalysis datasets, (a) ERA-Interim, (b) JRA-55, (c) MERRA, and (d) CFSR. The gray dashed and red solid lines represent the mean values under LS and HS conditions, while the corresponding shaded regions represent the 90% confidence intervals of the running averages.

Figures 1–3 suggest that the strongest solar signal is in the upper stratosphere. It is the region where the E-P fluxes and divergence exhibit large discrepancies among different reanalysis products (Lu et al. 2015; Martineau et al. 2016). It is important to check the robustness of the wave-forcing anomalies shown in Figs. 2 and 3 using other reanalysis datasets. Figure 4 shows the 31-day running averages of daily mean $\nabla \cdot \tilde{\mathbf{F}}$ from 1 October to 1 April at 35°–45°N and 3 hPa for both HS and LS conditions, calculated from four modern reanalysis products: ERA-Interim, MERRA, JRA-55, and CFSR. This region is chosen because the most significant $\nabla \cdot \tilde{\mathbf{F}}$ anomalies were found there and the anomalies had a sign reversal from positive to negative between early and late winter.

Under both HS and LS conditions all four reanalysis datasets show a similar seasonal development of $\nabla \cdot \tilde{\mathbf{F}}$ at 35°–45°N and 3 hPa. Namely, $\nabla \cdot \tilde{\mathbf{F}}$ becomes more negative from early October to late December and early January, then turning back toward zero thereafter. The structures of $\nabla \cdot \tilde{\mathbf{F}}$ are nearly identical in ERA-Interim, JRA-55, and CFSR except for their magnitudes. The solar anomalies are most significant in MERRA because the MERRA estimates are noticeably more variable under LS. Although the differences are not statistically significant in CFSR, all four reanalysis products show an unambiguous delay and deepening of the trough under HS. This contributes to the positive $\nabla \cdot \tilde{\mathbf{F}}$ anomalies in early winter and negative $\nabla \cdot \tilde{\mathbf{F}}$ anomalies in late winter. Figure 4 confirms that there are large uncertainties in wave-forcing estimates in the upper stratosphere. The uncertainty regarding solar-induced changes is mostly in the magnitude rather than the underlying difference in evolution. Thus, it remains worthwhile to search for the mechanism behind the delay. For simplicity and consistency, our results hereafter are entirely based on ERA-Interim.

b. *Changes in stratospheric waveguide*

In this section, solar modulation of the PV gradient $\overline{q}_\phi$ and the normalized refractive index $a^2 n_k^2$ for stationary waves are examined in relation to (i) changes in stratospheric waveguides, (ii) the PV gradient sharpening or

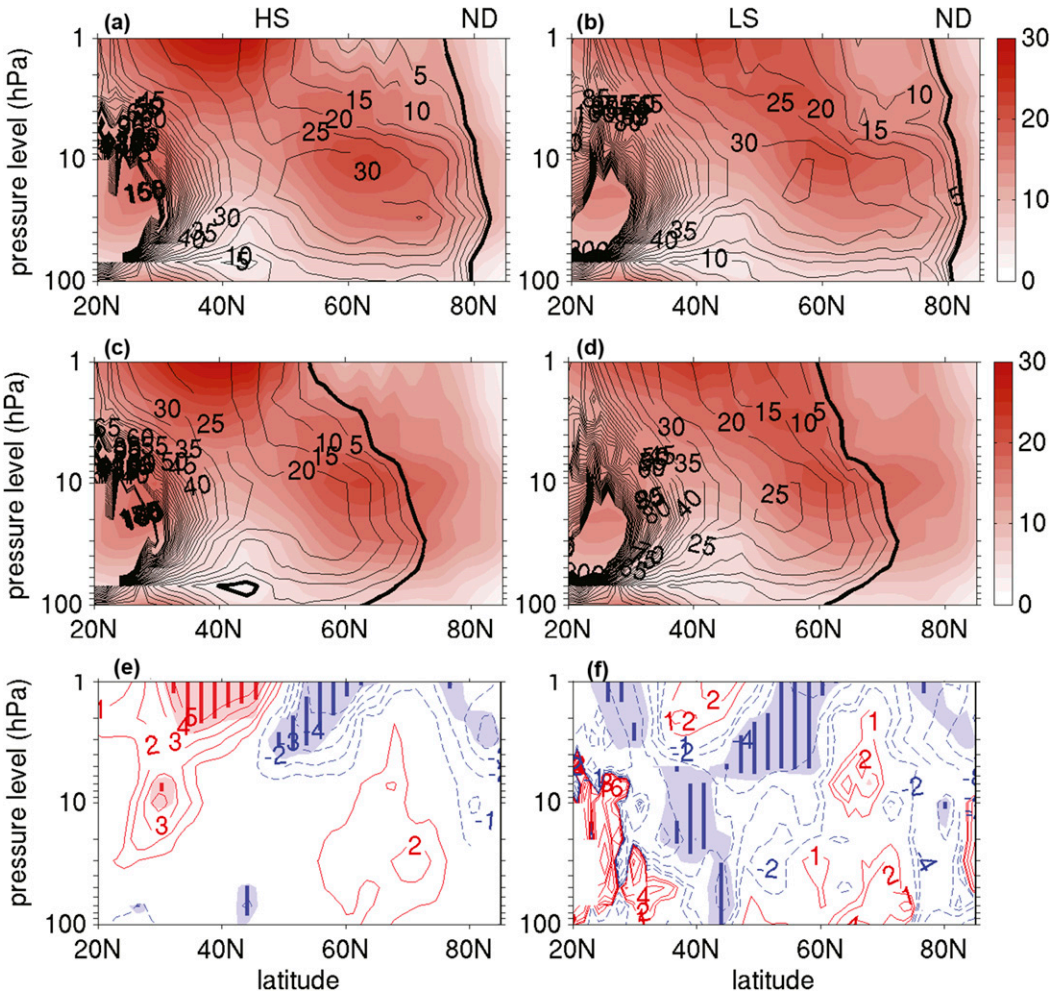

FIG. 5. November–December mean of the refractive index $a^2n_k^2$ with $k = 1$ (contours) and the PV gradient $\overline{q}_\phi$ (s^{-1}, shaded) under (a) HS and (b) LS conditions. (c),(d) As in (a),(b), but for $k = 2$. (e) Solar difference (HS − LS) of $\overline{q}_\phi$. (f) As in (e), but for the refractive index $a^2n_k^2$. The red and blue contours in (e) and (f) indicate positive and negative anomalies while the lightly shaded area and the vertical solid lines indicate p value ≤ 0.1 and 0.05 of the differences, respectively, all displayed in latitude–pressure height cross section of the stratosphere (20°–85°N, 1–100 hPa).

PV mixing concerning BPWs, and (iii) the formation of the stratospheric wave cavity.

Figures 5a,b show the November–December-averaged meridional PV gradient $\overline{q}_\phi$ (shaded) and refractive index $a^2n_k^2$ (contours) for wavenumber 1 (i.e., $k = 1$) under LS and HS conditions. Figures 5c,d are the same except for wavenumber 2 (i.e., $k = 2$). Figures 5e,f show their corresponding composite differences (i.e., HS − LS), which are applicable for both $k = 1$ and $k = 2$.

The climatology of the meridional PV gradient is marked by strongly positive values of $\overline{q}_\phi$ near the edge of the polar vortex with smaller values of $\overline{q}_\phi$ in the subtropics and at high latitudes (see Fig. 1 for jet location). A similar feature holds for $a^2n_k^2$ as well. Planetary waves tend to propagate along the region with large positive $\overline{q}_\phi$ and $a^2n_k^2$ while regions with small or negative values indicate reduced wave propagation, wave transience, or wave breaking (Matsuno 1970). As such, Figs. 5a–d indicate that the waves are guided along the edge of the polar vortex. While $\overline{q}_\phi$ is independent of wavenumber, the region with negative $a^2n_k^2$ expands more toward lower latitudes with increasing wavenumber k. Thus, stationary waves with zonal wavenumber 1 (wave 1) are more likely to propagate into the high-latitude stratosphere than the stationary waves with zonal wavenumber 2 (wave 2). Note that $a^2n_k^2$ becomes infinitely large in the vicinity of the subtropical zero-wind line (i.e., the thick black line in Figs. 1a,b), where wave absorption occurs.

Solar-cycle modulation of the stratospheric PV gradient is characterized by an equatorward shift of the region with large positive $\overline{q}_\phi$ in the upper stratosphere as $\overline{q}_\phi$ becomes more positive at 25°–45°N and more negative at 45°–60°N under HS (Fig. 5e). The reduction of $\overline{q}_\phi$ at 45°–60°N and 1–3 hPa involves significantly more negative values of $\overline{q}_\phi$ during December. This signifies that enhanced PV mixing in this region resulted in localized barotropic instability, which may lead to enhanced in situ wave generation (Kuo 1949). Nonlinear wave growth leads to enhanced wave breaking in the polar upper stratosphere; enhanced downward wave reflection follows because of the formation of a reflecting surface (Lu et al. 2017).

Figure 5f shows that solar modulation of the refractive index $a^2n_k^2$ is dominated by the negative anomalies near the stratospheric surf zone at 35°–45°N and at the flanks of the upper-stratospheric westerly jet. As such, these anomalies indicate a more confined cavity for stationary wave propagation under HS. These $a^2n_k^2$ anomalies differ from those shown in Fig. 5e because of the nonlinear operation between the PV gradient $\overline{q}_\phi$ and the zonal-mean wind $\overline{u}$ [i.e., the first term of Eq. (3)]. Nonlinear critical layer and BPWs are mainly responsible for such differences (Stewartson 1977; McIntyre and Palmer 1983; Waugh and Dritschel 1999).

To appreciate the seasonal development of solar-induced changes in BPWs, the 31-day running averages of $\overline{q}_\phi$ from 1 November to 1 April are shown in Figs. 6a–c for two regions in the upper stratosphere. The temporal evolution of $\overline{q}_\phi$ in region 1 at 30°–45°N and 1–2 hPa is characterized by a double-peak structure under both HS and LS conditions (see Fig. 6b). It is evident that $\overline{q}_\phi$ is generally greater with a noticeable delay of the seasonal development of $\overline{q}_\phi$ under HS than LS. This is associated with a prolonged development of the early-winter upsurge of $\overline{q}_\phi$ from mid-November to mid-December under HS. Such a delay leads to the separation of the 31-day-averaged $\overline{q}_\phi$ between HS and LS conditions (significant at 90% confidence interval) during mid-December–mid-January and in early March.

The temporal evolution of $\overline{q}_\phi$ in region 2 at 45°–90°N and 1–2 hPa is again characterized by a double-peak structure under both HS and LS conditions (Fig. 6c). However, $\overline{q}_\phi$ is generally smaller with a noticeable delay and deepening of the seasonal development under HS. The delay and deepening lead to the separations of the 31-day-averaged $\overline{q}_\phi$ between HS and LS conditions in December and February. It is worth noting that the peaks of the 31-day running averages of $\overline{q}_\phi$ in region 1 coincide with the troughs in region 2 under both HS and LS conditions. These are typically observed during BPW events in the upper stratosphere whereby an increase in the PV gradient near the center of the upper-stratospheric westerly jet is accompanied by enhanced mixing of the PV, indicated by the flattened PV gradients at higher latitudes (Polvani and Saravanan 2000). Given $\overline{q}_\phi$ is generally greater under HS than LS at 30°–45°N but the opposite holds at 46°–90°N, Figs. 6a–c thus suggest enhanced BPWs in the upper stratosphere under HS.

A typical stratospheric wave cavity has two vertically oriented reflecting surfaces, one in the midlatitudes and one in the polar region, and a horizontally oriented reflecting surface in the upper stratosphere (Harnik and Lindzen 2001). Because of the second term in Eq. (3), the reflecting surface in the polar region is always present. The approximate locations of the other two reflecting surfaces are indicated in Fig. 6d. Region 3 at 35°–50°N and 3–70 hPa represents the vertically oriented partial reflecting surface, which acts as a barrier for the equatorward-propagating stationary waves (Matsuno 1970). The reflecting surfaces are normally produced by BPWs, which involve an alternating absorption–reflection–overreflection nonlinear critical layer with the waves propagating in the meridional direction (McIntyre and Palmer 1983; Plumb 2010). Region 4 at 50°–90°N and 1–3 hPa represents the horizontally oriented partial reflecting surfaces, which acts to trap upward-propagating stationary waves. Upper-level BPWs and breaking gravity waves lead to downward wave reflection (Albers and Birner 2014). From Fig. 5, we can see that both $\overline{q}_\phi$ and $a^2n_k^2$ are climatologically small in these two regions. Thus, they are the regions where BPWs are most likely to occur climatologically. A reduction of $a^2n_k^2$ in these regions leads to enhanced wave breaking and/or internal reflection. According to Plumb (2010), we would also expect the increased likelihood of resonance if more waves are trapped internally within the stratosphere.

The seasonal development of $a^2n_1^2$ in region 3 is marked by a decline in $a^2n_1^2$ from early November to late December and an increase in $a^2n_1^2$ thereafter (Fig. 6e). During November–December, $a^2n_1^2$ is significantly smaller under HS, indicating reduced equatorward propagation of stationary waves through the stratospheric surf zone. A widening of the stratospheric surf zone via BPWs would lead to a poleward shift of the stratospheric waveguide, which guides the waves to propagate along the high-latitude route (Plumb 2010; Albers and Birner 2014).

The seasonal development of $a^2n_1^2$ in region 4 is marked by the noticeably smaller values of $a^2n_1^2$ from mid-November to early February under HS. The differences in the seasonally averaged $a^2n_1^2$ between HS and LS conditions become statistically significant in

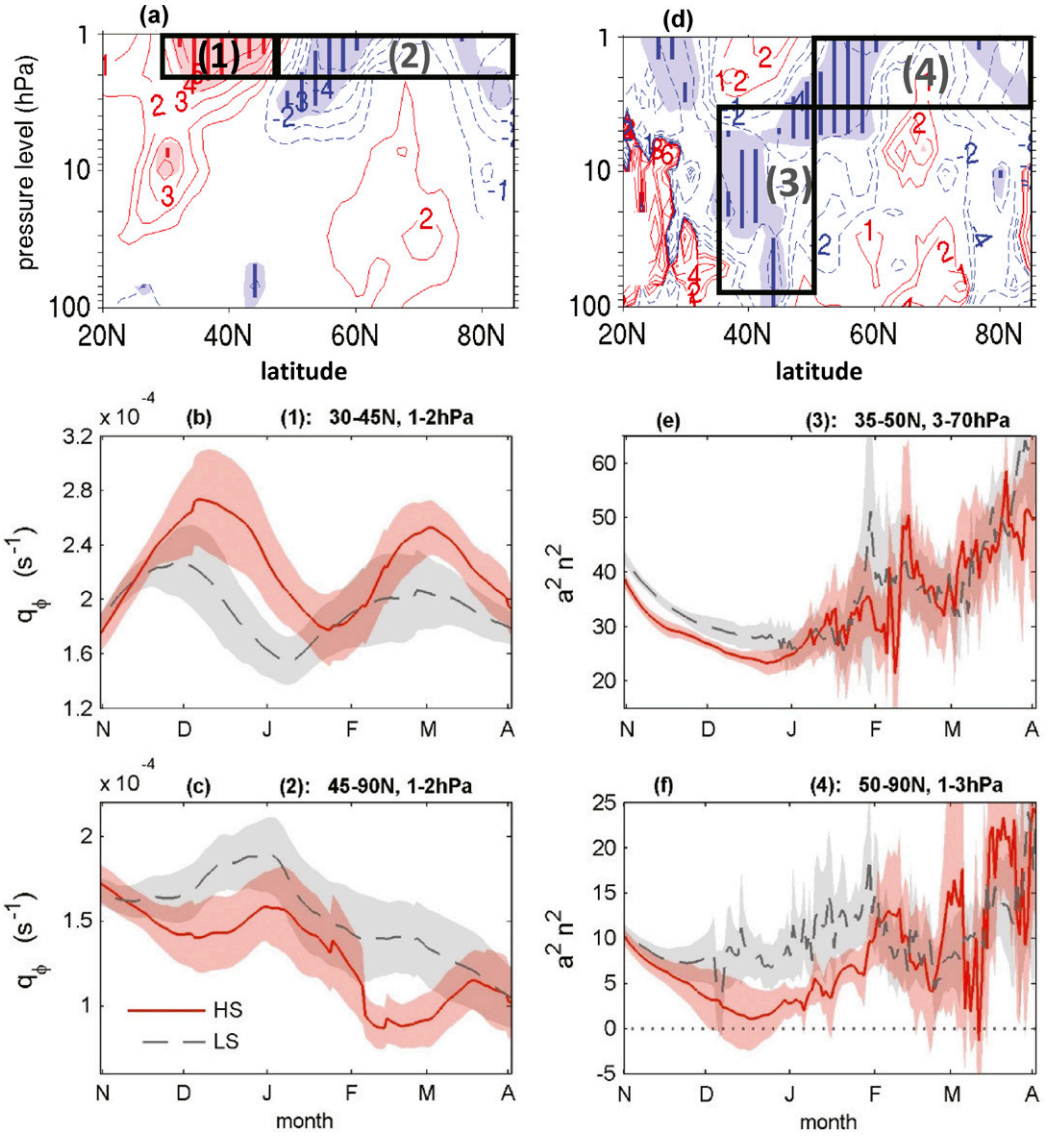

FIG. 6. (a) As in Fig. 5e with two black boxes added to show the key regions where 31-day running averages of the PV gradient $\overline{q}_\phi$ are taken and (b),(c) the corresponding area-averaged $\overline{q}_\phi$ under HS and LS conditions for the regions in (a). (d) As in Fig. 5f with two black boxes indicating the key regions where 31-day running averages of the wave-1 refractive index $a^2n_1^2$ are taken and (e),(f) the corresponding area-averaged $a^2n_1^2$ under HS and LS conditions for the regions in (b). The gray dashed and red solid lines represent the mean values under HS and LS conditions, while the corresponding shaded regions represent the 90% confidence intervals of the mean.

December–January according to their 90% confidence intervals. Note also that the 90% confidence interval dips into negative territory during December under HS while it remains mostly positive under LS. This implies reduced upward propagation of stationary wave 1 owing to enhanced BPWs, which may be followed by downward wave reflection (Matsuno 1970; Harnik and Lindzen 2001; Lu et al. 2017). Because the anomalies are the same for other wavenumbers (not shown), Figs. 6d–f thus imply reduced equatorward and upward propagation of stationary waves in early and midwinter under HS.

c. *Seasonal evolution of planetary wave responses*

In this section, we examine the solar-cycle modulation of BPWs based on wavenumber-dependent E-P flux and divergent anomalies. We discuss how these anomalies may play a role in forming the partial reflecting surfaces and how such an enhancement may lead to a seasonal delay of the net wave forcing on the polar vortex.

Figures 7a,b show the early- and late-winter climatological wave-1 E-P fluxes $\tilde{\mathbf{F}}_{\mathrm{PW1}} = [\tilde{F}^{(\phi)}_{\mathrm{PW1}}, \tilde{F}^{(z)}_{\mathrm{PW1}}]$ (arrows) and divergence $\nabla \cdot \tilde{\mathbf{F}}_{\mathrm{PW1}}$ (contours), which are similar to those of the total field (see Figs. 2a,b). This suggests that wave 1 plays a dominant role climatologically.

Figures 7c–g show the 2-month running averages of wave-1 composite differences from October–November to December–January, whereas Fig. 7h is the same but for January–March mean. The early to midwinter solar signal in wave 1 starts with the positive $\nabla \cdot \tilde{\mathbf{F}}_{\mathrm{PW1}}$ anomalies at 45°–60°N and 3–7 hPa as a result of poleward wave refraction from the westerly jet. The effect is followed by the negative $\nabla \cdot \tilde{\mathbf{F}}_{\mathrm{PW1}}$ anomalies poleward of 65°N at 1–3 hPa and at about 35°–45°N and 7–20 hPa. These negative $\nabla \cdot \tilde{\mathbf{F}}_{\mathrm{PW1}}$ anomalies are featured throughout the winter but are most significant during November–January. As the winter progresses, the divergent anomalies near the polar vortex edge and the convergent anomalies in the stratospheric surf zone move gradually downward. The effect is then followed by an increase in the upward wave-1 propagation in January–March. These wave-1 E-P flux anomalies indicate enhanced BPWs under HS because 1) they are located in the polar upper stratosphere and in the surf zone where BPWs normally occur (Albers and Birner 2014; McIntyre and Palmer 1983), 2) positive values of $\nabla \cdot \tilde{\mathbf{F}}_{\mathrm{PW1}}$ anomalies are found near the polar vortex edge, and 3) the associated E-P flux vectors are manifest as meridional divergence from the edge of the polar vortex as typically seen during a BPW event (Polvani and Saravanan 2000; Esler and Matthewman 2011). Their late-winter development is also similar to results from idealized studies regarding how BPWs act to precondition the SSWs (Waugh and Dritschel 1999).

It is worth noting that the negative $\nabla \cdot \tilde{\mathbf{F}}_{\mathrm{PW1}}$ anomalies in the midstratospheric surf zone disappear in $\nabla \cdot \tilde{\mathbf{F}}_{\mathrm{total}}$ (see Fig. 2c,d), due to a cancellation effect of poleward-propagating transient wave anomalies with zonal wavenumbers 2 and 3 reflecting from the region with negative $\nabla \cdot \tilde{\mathbf{F}}_{\mathrm{PW1}}$ anomalies (not shown). This effect is very similar to the idealized study of Haynes (1989) who show that barotropic instability leads to a large increase in the time-integrated wave absorptivity within the critical layers. The absorption is strongest for ultralong planetary waves. Higher wavenumber waves emit and propagate meridionally away from the critical layer as the flow rearranges itself locally. Such nonlinear critical-layer interaction is accompanied by little change in the background zonal-mean flow.

Figure 8a shows the climatological E-P fluxes (arrows) and divergence (contours) for November–March-averaged stationary wave 2, which is marked by the upward- and equatorward-propagating E-P fluxes at 40°–70°N with strong convergence centered near the stratospheric polar vortex.

During November–mid-January, the solar composite differences in $\nabla \cdot \tilde{\mathbf{F}}_{\mathrm{SPW2}}$ (Figs. 8b,c) are marked by the divergent anomalies at 40°–70°N, because of a reduction of upward-propagating waves from the troposphere. The divergent effect starts in the upper stratosphere and then descends downward into the troposphere. Without the aforementioned wave-1 anomalies, these stationary wave-2 anomalies would correspond to a downward movement of westerly wind anomalies, as reported by earlier studies (i.e., Kodera and Kuroda 2002). The circulation anomalies in the mid- and lower stratosphere during 1979–2014 are however not statistically significant at the $p = 0.05$ level. This is likely due to the enhanced BPWs and associated internal wave reflection, which make the westerly winds around the polar vortex less zonal under HS.

Figure 8d is the same as Figs. 8b,c except for the 61-day period from 16 January to 16 March. It shows that the E-P flux and the divergent anomalies of stationary wave 2 reverse their direction and sign in late winter with convergent anomalies along the polar vortex edge and the equatorward- and upward-propagating E-P flux anomalies originating from the high-latitude stratosphere and from the troposphere. Divergent anomalies are found in the subtropical upper stratosphere at 15°–25°N and 1–3 hPa with the poleward-pointing E-P flux anomalies, indicating reduced wave absorption near the subtropical zero-wind line. These late-winter wave forcing anomalies suggest enhanced wave disturbance under HS, which is consistent with the circulation anomalies shown in Figs. 1d,f.

d. Wave reflection and resonance

Internal normal modes readily radiate their energy into the upper stratosphere and mesosphere without imposing a drag on the mean flow (Salby 1984). However, once trapped, some of the transient waves may interact with quasi-stationary planetary waves and the polar vortex whereby they become excited as a result of resonance (Tung 1979; Tung and Lindzen 1979a,b; Plumb 1981, 2010). While their phase speeds shift to match those of stationary waves, their amplitudes grow and become sufficiently large. When they break, an SSW may be triggered as a result. In this section, evidence is provided to suggest that the enhanced stationary wave-2 forcing in late winter could be due to resonant excitation of internally reflected waves.

Figure 9a shows the climatology (contours) and solar composite differences (shaded) of November–February-averaged planetary wave momentum flux

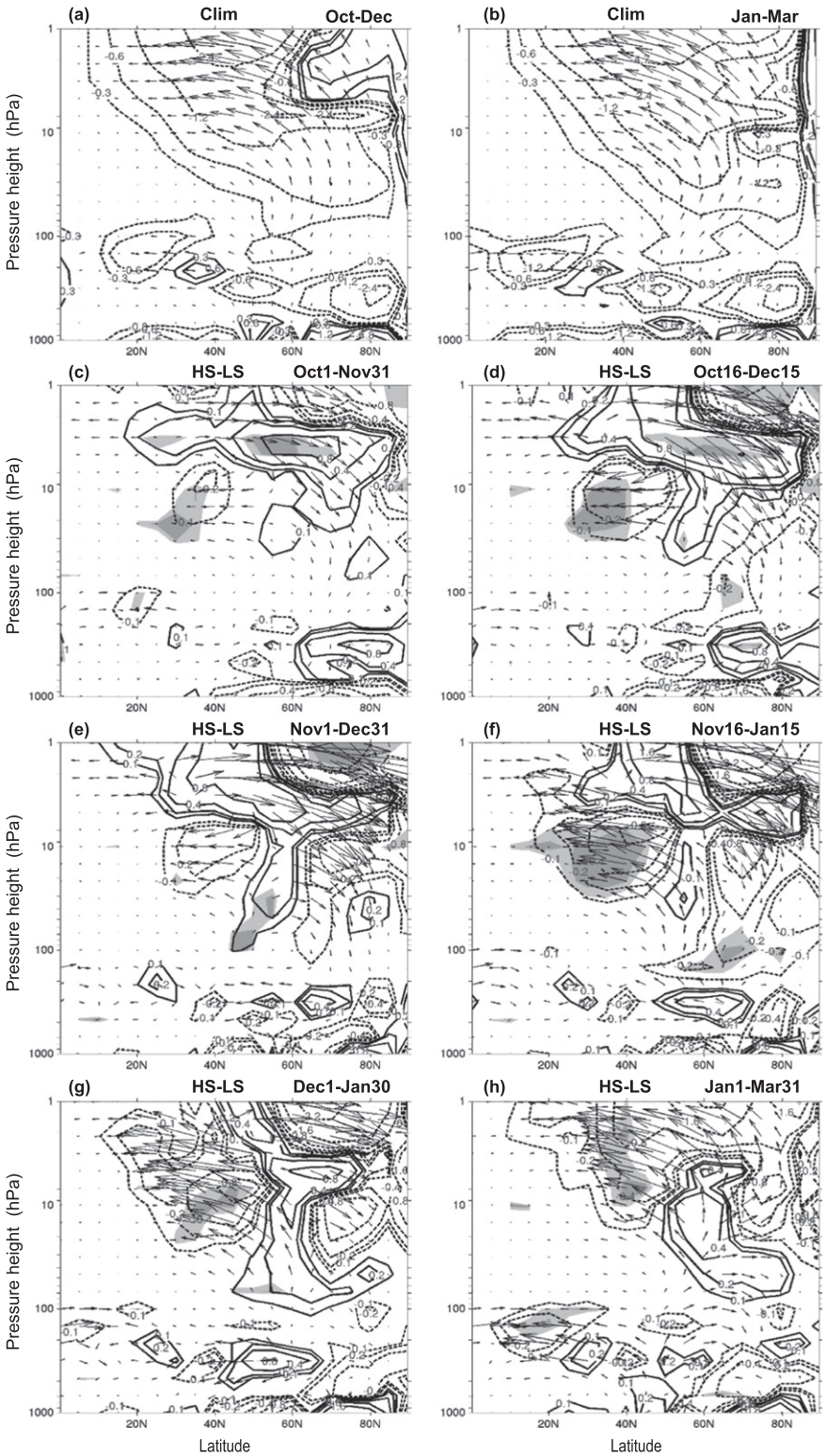

FIG. 7. (a),(b) As in Fig. 2a,b, but for wave 1. (c)–(g) Running 2-month averages of the solar composite differences in wave 1 from November to January. (h) As in (c), but for the January–March average. The arrows, contours, shading, and scaling applied to the E-P fluxes and anomalies are as in Fig. 2.

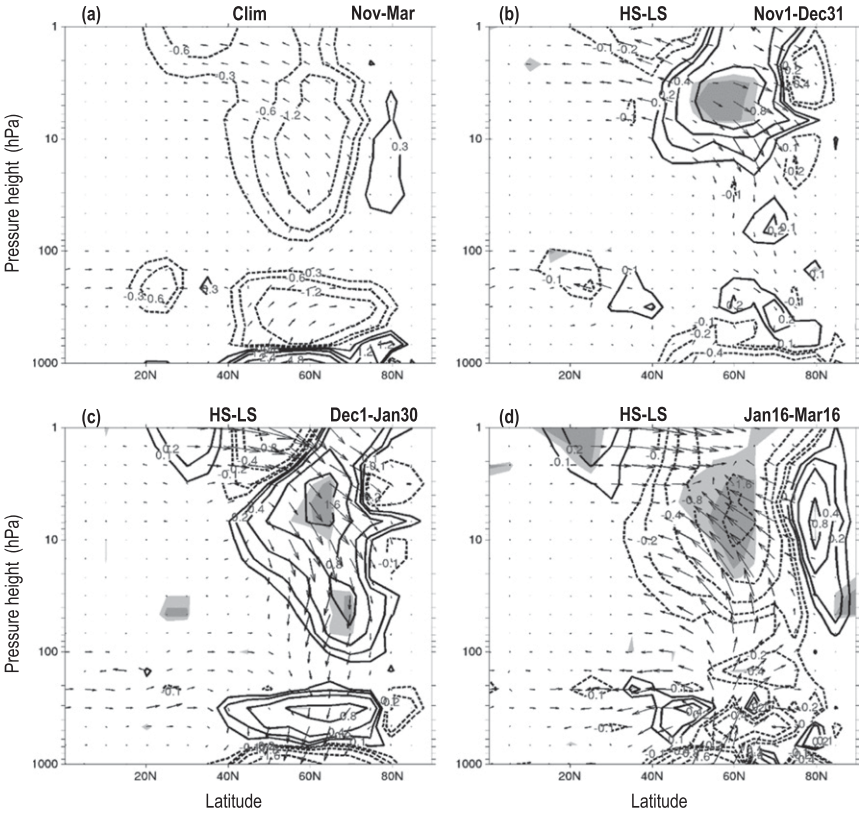

FIG. 8. (a) The November–March climatological-mean E-P fluxes (arrows) and E-P flux divergence (contours) of stationary wave 2. The 2-month averages of solar composite differences in stationary wave 2 of (b) November–December, (c) December–January, and 16 January–16 March. The arrows, contours, shading, and scaling applied to the E-P fluxes and anomalies are as in Fig. 2. Note that the E-P flux vectors of the anomalies are larger in size compared to the climatology because the anomalies are multiplied by a factor of 10.

$\overline{u'v'}$ estimated from daily data. The climatology is marked by positive $\overline{u'v'}$ (i.e., equatorward wave propagation) in the mid-to-upper stratosphere and in the subtropical to midlatitude troposphere, with negative $\overline{u'v'}$ (i.e., poleward propagation) in the high-latitude lower stratosphere and tropical upper troposphere. The solar signal in the seasonal-mean $\overline{u'v'}$ is marked by significant positive anomalies at 25°–45°N and 5–30 hPa. These anomalies indicate enhanced equatorward wave propagation near the stratospheric surf zone, in association with enhanced BPWs under HS.

Figure 9b is similar to Fig. 9a except that the seasonal averages include those days when a negative $\overline{u'v'}$ occurred. As expected, the climatology is all negative. Climatologically, poleward wave reflection occurs in the regions where large negative values are found (i.e., in the tropical upper troposphere and at high latitudes). The solar signal is marked by negative anomalies in the high-latitude stratosphere at 60°–80°N and 2–20 hPa, suggesting enhanced poleward reflection or refraction at high latitudes under HS. These anomalies contribute to enhanced BPWs in the polar upper stratosphere (see Fig. 7).

Figures 9c,d are similar to Figs. 9a,b but for the planetary wave heat flux $\overline{v'T'}$. The climatology of the seasonal-mean $\overline{v'T'}$ is largely positive except for a small region in the subtropical upper troposphere (Fig. 9c). This indicates that upward wave propagation dominates the winter circulation in terms of climatology. The solar signal in the seasonal-mean $\overline{v'T'}$ is marked by the positive anomalies at 20°–40°N and 2–7 hPa, indicating enhanced upward planetary wave propagation there under HS, consistent with an equatorward shift of the waveguide in the upper stratosphere (see Fig. 5).

The climatology of seasonal-mean negative daily $\overline{v'T'}$ is again everywhere negative. The regions with strongest internal wave reflection include the tropical upper troposphere and high latitudes, where large negative values of $\overline{v'T'}$ exist. These regions are prone to internal wave reflection climatologically because poleward wave

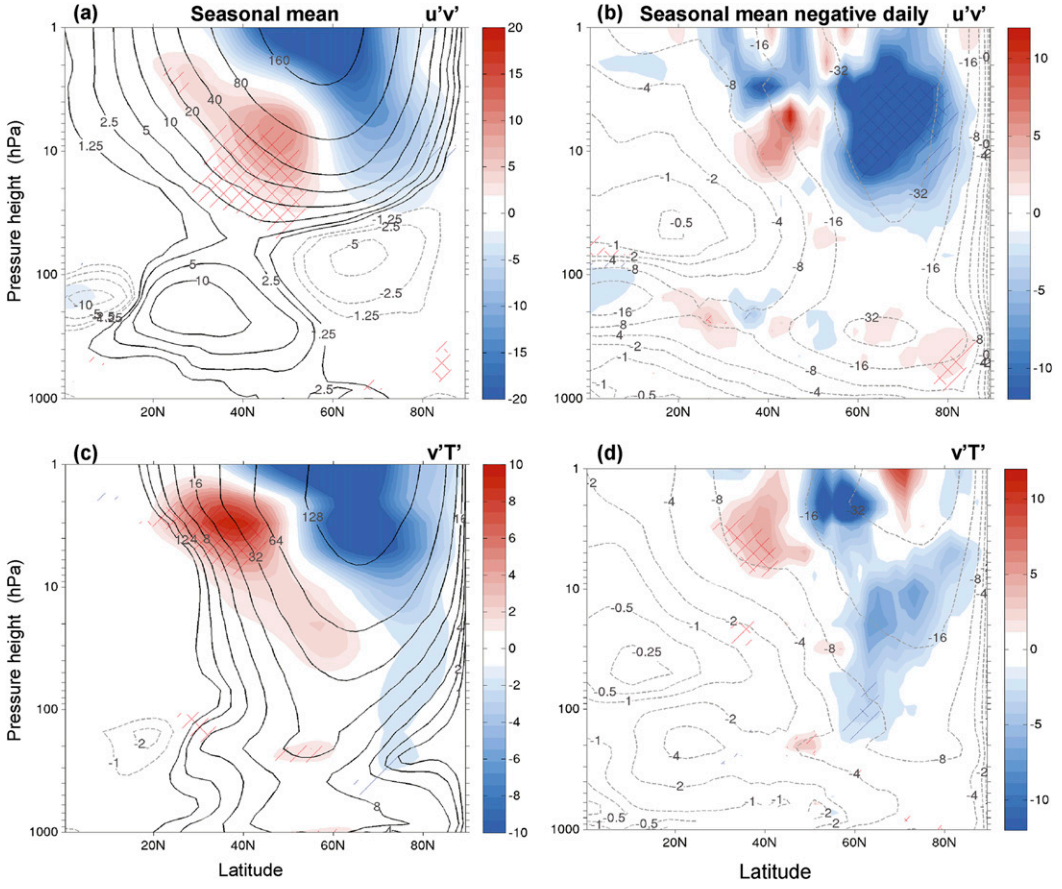

FIG. 9. (a) Climatology (contours) and solar composite difference (HS − LS; shaded) of November–February mean momentum flux $\overline{u'v'}$ of planetary waves ($m^2 s^{-2}$). (b) As in (a), but only includes those days when a negative $\overline{u'v'}$ occurred at each latitude and pressure location. (c),(d) As in (a), (b), but for heat flux $\overline{v'T'}$ (K m s^{-1}). The hatching and cross hatching indicate that the differences are statistically significant at p value ≤ 0.1 and 0.05, respectively.

reflection also peaks in these regions (see Fig. 9d). The solar signal is marked by positive anomalies at 30°–45°N and 2–5 hPa and negative anomalies at about 60°N and 70–200 hPa, indicating enhanced downward wave reflection at high latitudes with reduced downward wave reflection near the westerly jet center. Solar-cycle modulation of BPWs is initialized in the uppermost stratosphere. Figure 9 suggests an equatorward shift of planetary wave propagation in the upper stratosphere with enhanced downward and poleward wave reflection at high latitudes.

In section 3c, we stated that there is substantial cancellation between the solar signal in wave 1 and wave 2 near the region with enhanced wave-1 absorption. We suggested that these E-P flux anomalies and their cancellation are indicative of enhanced BPWs with enhanced poleward wave reflection. To provide further evidence for enhanced poleward wave reflection, Figs. 10 and 11 extend the analysis shown in Fig. 9 by only including planetary waves with zonal wavenumbers 2 and 3. Figure 10a is similar to Fig. 9d but for wavenumbers 2 and 3 during December–February. It shows that the solar signal in midwinter is marked by positive anomalies of seasonal averages of negative daily $\overline{v'T'}$ at 35°–45°N and 1–5 hPa, indicating reduced downward reflection near the upper-stratospheric westerly jet. Negative anomalies are found at 65°–80°N and 7–30 hPa, suggesting enhanced downward reflection in the high latitudes. Consistent with these anomalies, the opposite-signed anomalies of the frequency occurrence of negative daily $\overline{v'T'}$ are found in the corresponding regions (Fig. 10b). Thus, Fig. 10 suggests that downward wave reflection has shifted from the subtropics to the high latitudes under HS. This is consistent with the downward wave reflection observed and reported recently by Lu et al. (2017).

Figure 11 is similar to Fig. 9b but for wavenumbers 2 and 3 and for the 2-month running averages from November to March. The climatology resembles that of the total planetary waves (see Fig. 9b), suggesting that

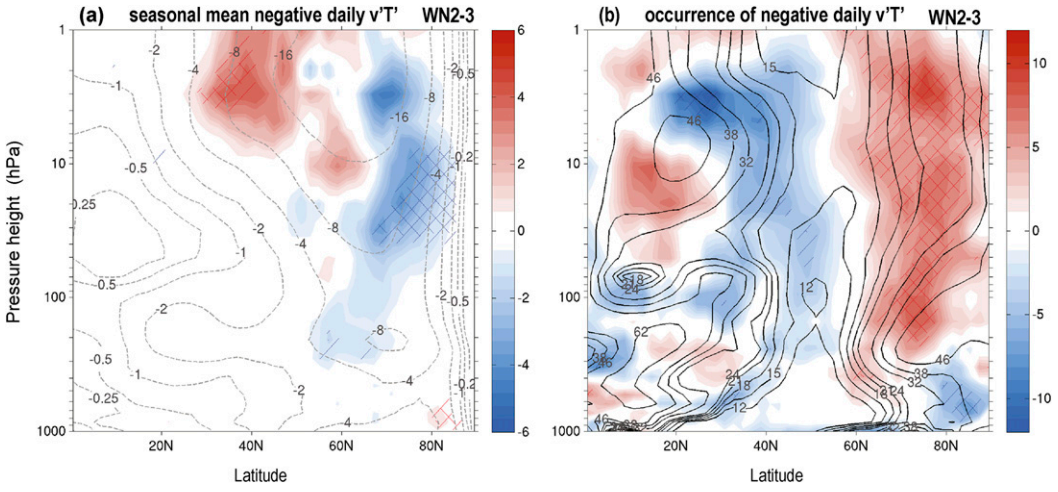

FIG. 10. (a) Climatology (contours) and solar composite difference (HS − LS; shaded) of December–February-averaged heat flux $\overline{v'T'}$ (K m s^{-1}) for planetary waves with zonal wavenumbers 2 and 3 only. (b) Climatology (contours) and solar composite difference (HS − LS; shaded) of the number of days during which negative daily mean $\overline{v'T'}$ of planetary waves with zonal wavenumbers 2 and 3 occurred. The hatching and cross hatching indicate that the differences are statistically significant at p value ≤ 0.1 and 0.05, respectively.

climatological poleward reflection of wavenumbers 2 and 3 takes place primarily at high latitudes. A solar modulation of the seasonally averaged negative daily $\overline{u'v'}$ is marked by the regions with negative anomalies (i.e., blue-shaded regions), indicating enhanced poleward wave reflection under HS. Negative anomalies first appear at 55°–70°N and 5–20 hPa in November–December and then move poleward and downward as the winter progresses. From midwinter they become persistently strong and statistically significant in the high-latitude lower stratosphere. Thus, these results suggest that the reduced upward-propagating wavenumbers 2 and 3 at 30°–45°N and 1–5 hPa (see Fig. 10) is due to enhanced poleward reflection of wavenumbers 2 and 3 below in the mid-to-lower stratosphere.

Figure 12 provides evidence to suggest that solar-cycle modulation of internal wave reflection may lead to resonant growth of transient wavenumbers 2 and 3 in midwinter. It shows the latitudinal distributions of the wave power (in units of m^2) of waves with zonal wavenumbers 2 and 3 and with a period of 10 days at 10 hPa. The wave power is detected and estimated using the Hayashi spectra method and daily geopotential height

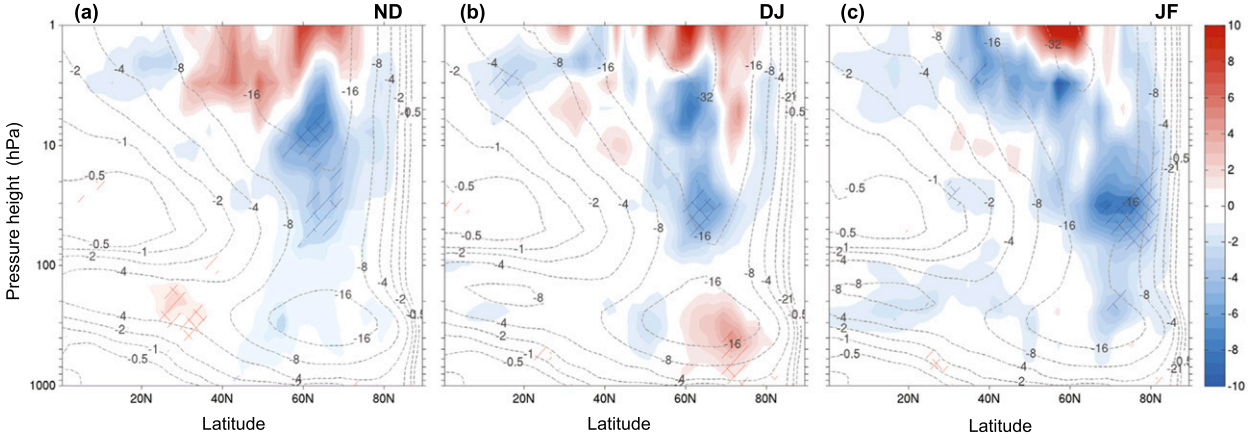

FIG. 11. (a)–(c) Running 2-month averages of the seasonal averages of $\overline{u'v'}$ for planetary waves with zonal wavenumbers of 2 and 3 from November to February. As in Fig. 9b, the averages include only those days during which a negative daily mean $\overline{u'v'}$ of the planetary waves with zonal wavenumbers of 2 and 3 occurred. The hatching and cross hatching indicate that the differences are statistically significant at p value ≤ 0.1 and 0.05, respectively.

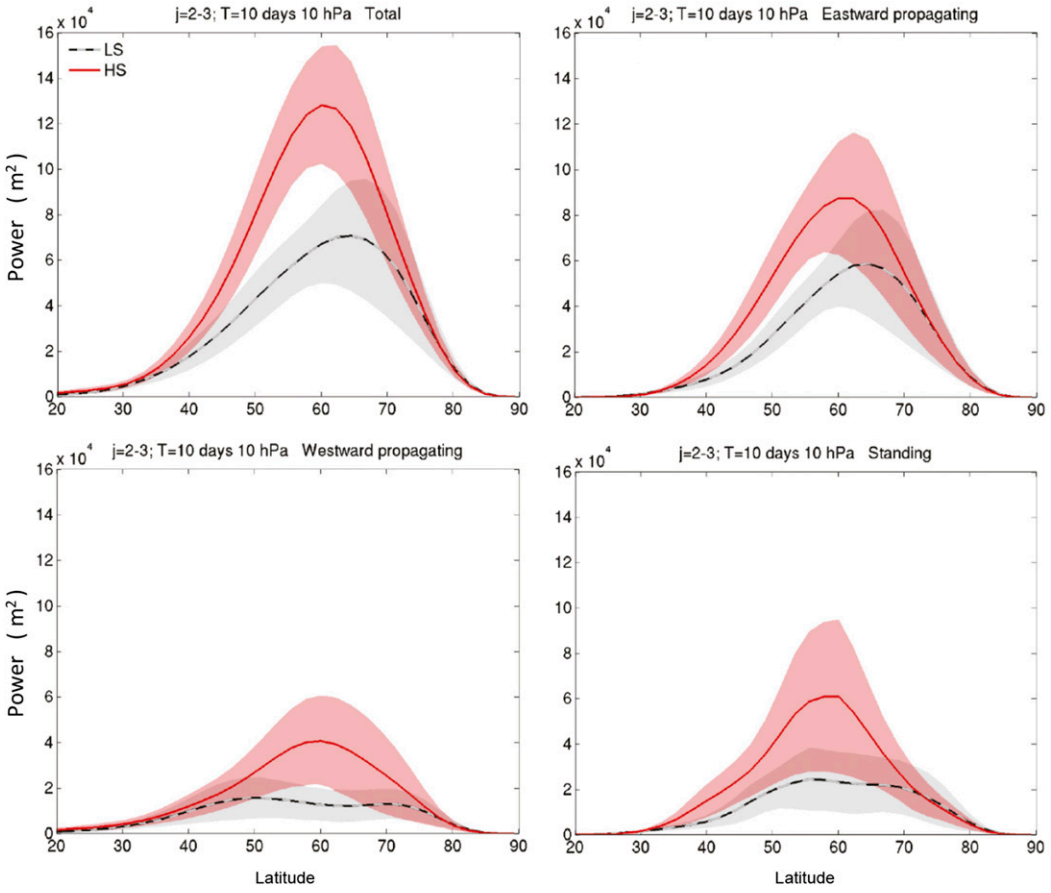

FIG. 12. Spectra power (m^2) of the transient planetary waves with zonal wavenumbers of 2 and 3 and a period of approximately 10 days of (top left) total, (top right) eastward-propagating, (bottom left) westward-propagating, and (bottom right) standing waves as a function of latitude (20°–90°N) at 10 hPa and for the extended midwinter period of November–February. The gray dashed and red solid lines represent the mean values under HS and LS conditions, while the corresponding shaded regions represent the 90% confidence intervals of the mean.

field over the months of November–February. The greater the power, the larger the wave amplitudes. Similar results can also be obtained at the pressure height range of 5–30 hPa (not shown), suggesting that the effect is of stratospheric origin and is linked to the enhanced BPWs in the stratospheric surf zone at 35°–45°N.

It is evident that these transient wavenumbers 2 and 3 are significantly enhanced for the total, eastward- and westward-propagating waves under HS. The enhancement of eastward-propagating waves is most significant at 40°–60°N where the wave-1 BPWs are enhanced (see Fig. 7). Figure 12 (top right) implies that eastward-propagating transient waves with zonal wavenumbers 2 and 3 and at 10-day period are anomalously generated and/or reflected from the regions with enhanced BPWs. Figure 12 (bottom left) shows that the enhancement of westward propagation is however found at 55°–65°N, where the polar vortex edge is located. While the amplitudes of the westward-propagating and standing wave components are rather small under LS (see Fig. 12, bottom), they become noticeably greater than zero under HS. Together, Fig. 12 indicates that higher solar activity leads to enhanced poleward reflection of transient wavenumbers 2 and 3 from the stratospheric surf zone. Resonant excitation is expected as a result of counterpropagating waves or enhanced overreflection (Harnik and Heifetz 2007). Once these waves become internally trapped in the stratosphere, a constructive interference could lead to resonance. Based on these results, we propose that resonance offers a possible explanation for the enhanced stationary wavenumbers 2 and 3 in late winter (see Fig. 8d).

4. Conclusions and discussion

This study provides evidence to suggest that the 11-yr solar cycle modulates the seasonal development of the northern winter stratosphere by affecting breaking

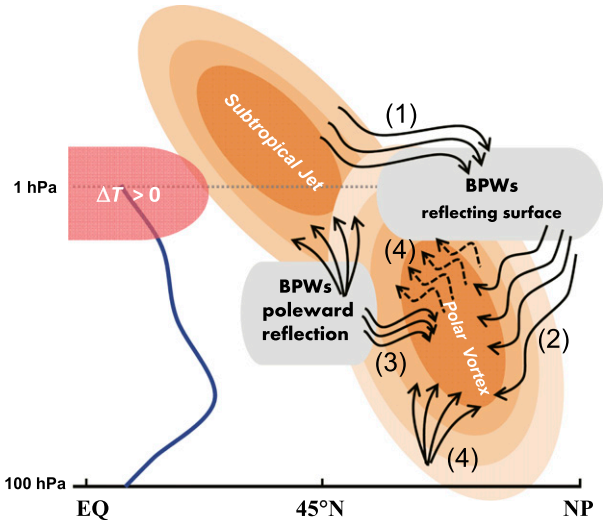

FIG. 13. Schematic diagram showing the sequence of steps (1–4) that contribute to the sign reversal of stratospheric circulation anomalies for higher solar forcing. The red half oval represents solar UV enhanced temperature anomalies while orange-shaded ovals indicate the upper-stratospheric subtropical westerly jet and the stratospheric polar vortex. These two jets would become more separated under HS than LS conditions. The gray-shaded regions represent the regions with enhanced BPWs and internal wave reflection. The solid streamlines indicate enhanced planetary wave propagation. The dashed streamlines indicate resonant wave disturbances. The subtropical zero-wind line is shown with the blue curve. See text for detailed explanations.

planetary waves (BPWs), internal wave reflection, and resonance. Based on ERA-Interim for the period of 1979–2014, we find that four key sequential steps are involved regarding the dynamical responses to enhanced solar forcing during boreal winter, as illustrated in Fig. 13. The chain of events is expanded below.

1) The enhanced solar UV forcing in the upper stratosphere leads to changes in upper-stratospheric temperature, winds, and waveguides in early winter. The chain of events starts with enhanced subtropical westerlies, which lead to enhanced poleward refraction of planetary waves at approximately 3 hPa. The changes above this level include an enhanced PV gradient $\overline{q}_\phi$ on the equatorward flank of the westerly jet at 30°–45°N, stronger wave breaking at high latitudes at 65°–90°N and much reduced $\overline{q}_\phi$ between these regions. Enhanced upper-level BPWs erode the PV gradient at 54°–60°N and 1–3 hPa, which becomes negative in December. Wave growth via barotropic energy transfer leads to an intensification of poleward wave reflection. Wave breaking at high latitudes results in a reflecting surface to form in the polar upper stratosphere.
2) Subsequent upward-propagating planetary waves are reflected downward into the mid- and lower stratosphere, where they are then deflected toward the lower latitudes. Enhanced equatorward wave propagation led to wave absorption at 35°–45°N and 5–20 hPa, resulting in a widening of the mid-stratospheric surf zone. Together with an equatorward shift of the upper-level waveguide, the stratospheric waveguide becomes constricted at about 45°–60°N and 5–10 hPa. Reduced upward wave propagation through the region results in a stronger upper-stratospheric westerly jet in early winter.
3) After January, the regions with enhanced BPWs in the polar upper stratosphere and the midstratospheric surf zone act as "barriers" for subsequent upward and equatorward wave propagation. As the waves entering the stratosphere become trapped internally within the stratosphere, anomalies of zonal wavenumbers 2 and 3 are generated and reflected poleward from the stratospheric surf zone with enhanced BPWs as a result of the incident waves rearranging the PV locally via a nonlinear critical layer (Haynes 1989). The poleward-reflected waves then interact with the polar vortex and the stationary waves propagating from the troposphere.
4) The poleward reflected transient wavenumbers 2 and 3 with certain phase speeds become resonantly excited near the polar vortex edge. Such an effect is signified by the counterpropagating 10-day transient wavenumbers 2 and 3. At the same time, the equatorial flank of the polar vortex at 5–20 hPa is gradually shaped by the enhanced BPWs. The stratospheric waveguide becomes more vertically aligned, guiding the waves to propagate upward and poleward along the high-latitude route. The combined effect is the presence of stronger wave disturbances that encompassed much of the extratropical upper stratosphere. This leads to a weaker and more disturbed upper-stratospheric westerly jet and downward moment of easterly wind anomalies in late winter.

The chain of events illustrated in Fig. 13 provides a mechanistic view regarding the observed sign reversal of the solar cycle signal, whereby HS − LS differences are characterized by a stronger and colder polar vortex in early winter and a more disturbed and warmer vortex in late winter. Here, the effect is explained as a delay and deepening of the seasonal development of stratospheric wave–mean flow interaction via enhanced BPWs, internal wave reflection, and resonance. The associated changes in stratospheric waveguide under HS disrupt the classic mechanism that involves the downward movement of zonal-mean anomalies via the cascade effect of wave breaking below a critical layer. It is

necessary to check the extent to which these processes are represented in climate models, given that the chain of events depends critically on BPWs in the uppermost stratosphere in early winter and nonlinear wave reflection from the midstratospheric surf zone in midwinter.

Idealized studies have shown that BPWs are sensitive to a range of factors, including meridional and vertical wind shears, the strength of the upward-propagating waves, axisymmetric boundary conditions, and model resolution (Waugh and Dritschel 1999; Polvani and Saravanan 2000; Walker and Magnusdottir 2003). In particular, the upper-stratospheric BPWs are manifestations of complicated interactions between the background flow and wave activity from the troposphere. The upper-level BPWs require the wave forcing from the troposphere to be relatively small (Waugh and Dritschel 1999). Also, to allow the partial wave cavity to form in midwinter, strong BPWs aloft should also be accompanied by a stable polar vortex below (Polvani and Saravanan 2000). The mechanisms illustrated in Fig. 13 could be interrupted by other processes. For instance, in the event when the lower-stratospheric QBO is in its easterly phase, the enhanced BPWs in the lower and middle stratosphere would lead to a reduction of the PV gradient along the polar vortex edge (White et al. 2015, 2016). These lower-level QBO-induced BPWs would then inhibit upward wave propagation, shielding the upper stratosphere from BPWs. This provides an explanation for the solar-cycle and QBO relationship observed earlier by Labitzke (1987) and the weakened Holton–Tan effect under HS conditions.

We emphasize that the data record used by this study covers only the period of 1979–2014, which is relatively short for studying an 11-yr perturbation. Perturbations in the stratosphere on decadal and multidecadal time scales may also be linked to changes in the troposphere, such as El Niño–Southern Oscillation (ENSO) or the Pacific decadal oscillation (PDO). The presence of these decadal variations could affect the reported solar signal. Because of the nonlinear coupling between the waves and the stratospheric mean flow, the dynamic response to the 11-yr solar UV variation may not be stationary for extended periods. Possible regime changes in either the tropospheric wave generation or the stratospheric background flow could result in characteristic and/or temporal variation of the BPWs. Decadal and multidecadal changes in these conditions would give rise to rather small or even a lack of solar signal in long-term averages either in observations or in model simulations. Given that our evaluation is constrained by the uncertainties in the reanalysis data, additional studies are needed to evaluate the robustness of the proposed mechanisms.

Acknowledgments. This study is funded by the British Antarctic Survey Polar Science for Planet Earth Programme and the National Centre for Atmospheric Science of the Natural Environment Research Council (NERC). It is also funded by the North Atlantic Climate System Integrated Study (ACSIS) (NE/N018028/1). We acknowledge using ERA-Interim (http://apps.ecmwf.int/datasets/data/interim-full-daily) for most of our analysis. Figure 4 was based on the daily zonal-mean fields made available by the SPARC Reanalysis Intercomparison Project (S-RIP; https://s-rip.ees.hokudai.ac.jp). We thank Adam A. Scaife, Tony Philips, John C. King, and three anonymous reviewers for constructive comments that helped to improve the clarity of the paper.

REFERENCES

Abatzoglou, J. T., and G. Magnusdottir, 2006: Planetary wave breaking and nonlinear reflection: Seasonal cycle and interannual variability. *J. Climate*, **19**, 6139–6152, doi:10.1175/JCLI3968.1.

Albers, J. R., and T. Birner, 2014: Vortex preconditioning due to planetary and gravity waves prior to sudden stratospheric warmings. *J. Atmos. Sci.*, **71**, 4028–4054, doi:10.1175/JAS-D-14-0026.1.

Andrews, D. G., J. R. Holton, and C. B. Leovy, 1987: *Middle Atmosphere Dynamics*. Academic Press, 489 pp.

Ball, W. T., J. D. Haigh, E. V. Rozanov, A. Kuchar, T. Sukhodolov, F. Tummon, A. V. Shapiro, and W. Schmutz, 2016: High solar cycle spectral variations inconsistent with stratospheric ozone observations. *Nat. Geosci.*, **9**, 206–209, doi:10.1038/ngeo2640.

Brasseur, G. P., and S. Solomon, 2005: *Aeronomy of the Middle Atmosphere*. D. Reidel Publishing Company, 445 pp.

Charney, J. G., and P. G. Drazin, 1961: Propagation of planetary-scale disturbances from the lower into the upper atmosphere. *J. Geophys. Res.*, **66**, 83–109, doi:10.1029/JZ066i001p00083.

Chiodo, G., N. Calvo, D. R. Marsh, and R. Garcia-Herrera, 2012: The 11-year solar cycle signal in transient simulations from the Whole Atmosphere Community Climate Model. *J. Geophys. Res.*, **117**, D06109, doi:10.1029/2011JD016393.

——, ——, ——, ——, N. Calvo, and J. Garca, 2014: On the detection of the solar signal in the tropical stratosphere. *Atmos. Chem. Phys.*, **14**, 5251–5269, doi:10.5194/acp-14-5251-2014.

Cnossen, I., H. Lu, C. J. Bell, L. J. Gray, and M. M. Joshi, 2011: Solar signal propagation: The role of gravity waves and stratospheric sudden warmings. *J. Geophys. Res.*, **116**, D02118, doi:10.1029/2010JD014535.

Dee, D. P., and Coauthors, 2011: The ERA-Interim reanalysis: Configuration and performance of the data assimilation system. *Quart. J. Roy. Meteor. Soc.*, **137**, 553–597, doi:10.1002/qj.828.

deToma, G., O. R. White, B. G. Knapp, G. J. Rottman, and T. N. Woods, 1997: Mg II core-to-wing index: Comparison of SBUV2 and SOLSTICE time series. *J. Geophys. Res.*, **102**, 2597–2610, doi:10.1029/96JA03342.

Dhomse, S. S., M. P. Chipperfield, R. P. Damadeo, J. M. Zawodny, W. T. Ball, W. Feng, R. Hossaini, G. W. Mann, and J. D. Haigh, 2016: On the ambiguous nature of the 11 year solar cycle signal in upper stratospheric ozone. *Geophys. Res. Lett.*, **43**, 7241–7249, doi:10.1002/2016GL069958.

Dritschel, D. G., 1986: The nonlinear evolution of rotating configurations of uniform vorticity. *J. Fluid Mech.*, **172**, 157–182, doi:10.1017/S0022112086001696.

Dunn-Sigouin, E., and T. A. Shaw, 2015: Comparing and contrasting extreme stratospheric events, including their coupling to the tropospheric circulation. *J. Geophys. Res. Atmos.*, **120**, 1374–1390, doi:10.1002/2014JD022116.

Edmon, H. J., B. J. Hoskins, and M. E. McIntyre, 1980: Eliassen–Palm cross sections for the troposphere. *J. Atmos. Sci.*, **37**, 2600–2616, doi:10.1175/1520-0469(1980)037<2600:EPCSFT>2.0.CO;2.

Ermolli, I., and Coauthors, 2013: Recent variability of the solar spectral irradiance and its impact on climate modelling. *Atmos. Chem. Phys.*, **13**, 3945–3977, doi:10.5194/acp-13-3945-2013.

Esler, J. G., and N. Matthewman, 2011: Stratospheric sudden warmings as self-tuning resonances. Part II: Vortex displacement events. *J. Atmos. Sci.*, **68**, 2505–2523, doi:10.1175/JAS-D-11-08.1.

Gray, L. J., S. Crooks, C. Pascoe, S. Sparrow, and M. Palmer, 2004: Solar and QBO influences on the timing of stratospheric sudden warmings. *J. Atmos. Sci.*, **61**, 2777–2796, doi:10.1175/JAS-3297.1.

——, and Coauthors, 2010: Solar influences on climate. *Rev. Geophys.*, **48**, RG4001, doi:10.1029/2009RG000282.

Haigh, J. D., 2003: The effects of solar variability on the Earth's climate. *Philos. Trans. Roy. Soc. London*, **361A**, 95–111, doi:10.1098/rsta.2002.1111.

Harnik, N. N., and R. S. Lindzen, 2001: The effect of reflecting surfaces on the vertical structure and variability of stratospheric planetary waves. *J. Atmos. Sci.*, **58**, 2872–2894, doi:10.1175/1520-0469(2001)058<2872:TEORSO>2.0.CO;2.

——, and E. E. Heifetz, 2007: Relating overreflection and wave geometry to the counterpropagating Rossby wave perspective: Toward a deeper mechanistic understanding of shear instability. *J. Atmos. Sci.*, **64**, 2238–2261, doi:10.1175/JAS3944.1.

Hayashi, Y., 1971: A generalized method of resolving disturbances in to progressive and retrogressive waves by space fourier and time cross-spectral analyses. *J. Meteor. Soc. Japan*, **49**, 125–128, doi:10.2151/jmsj1965.49.2_125.

Haynes, P. H., 1989: The effect of barotropic instability on the nonlinear evolution of a Rossby wave critical layer. *J. Fluid Mech.*, **207**, 231–266, doi:10.1017/S0022112089002569.

Hitchcock, P., and P. H. Haynes, 2016: Stratospheric control of planetary waves. *Geophys. Res. Lett.*, **43**, 11 884–11 892, doi:10.1002/2016GL071372.

Holton, J. R., and C. Mass, 1976: Stratospheric vacillation cycles. *J. Atmos. Sci.*, **33**, 2218–2225, doi:10.1175/1520-0469(1976)033<2218:SVC>2.0.CO;2.

Hood, L. L., and Coauthors, 2015: Solar signals in CMIP-5 simulations: The ozone response. *Quart. J. Roy. Meteor. Soc.*, **141**, 2670–2689, doi:10.1002/qj.2553.

Ineson, S., A. A. Scaife, J. R. Knight, J. C. Manners, N. J. Dunstone, L. J. Gray, and J. D. Haigh, 2011: Solar forcing of winter climate variability in the Northern Hemisphere. *Nat. Geosci.*, **4**, 753–757, doi:10.1038/ngeo1282.

Killworth, P. D., and M. E. McIntyre, 1985: Do Rossby-wave critical layers absorb, reflect, or over-reflect? *J. Fluid Mech.*, **161**, 449–462, doi:10.1017/S0022112085003019.

Kodera, K., and Y. Kuroda, 2002: Dynamical response to the solar cycle. *J. Geophys. Res.*, **107**, 4749, doi:10.1029/2002JD002224.

Kuo, H. L., 1949: Dynamic instability of two-dimensional nondivergent flow in a barotropic atmosphere. *J. Meteor.*, **6**, 105–122, doi:10.1175/1520-0469(1949)006<0105:DIOTDN>2.0.CO;2.

Labitzke, K., 1987: Sunspots, the QBO, and the stratospheric temperature in the north polar region. *Geophys. Res. Lett.*, **14**, 535–537, doi:10.1029/GL014i005p00535.

Lean, J., 2000: Evolution of the sun's spectral irradiance since the Maunder Minimum. *Geophys. Res. Lett.*, **27**, 2425–2428, doi:10.1029/2000GL000043.

Lu, H., D. Pancheva, P. Mukhtarov, and I. Cnossen, 2012: QBO modulation of traveling planetary waves during northern winter. *J. Geophys. Res.*, **117**, D09104, doi:10.1029/2011JD016901.

——, L. J. Gray, M. P. Baldwin, and M. J. Jarvis, 2009: Life cycle of the QBO-modulated 11-year solar cycle signals in the Northern Hemispheric winter. *Quart. J. Roy. Meteor. Soc.*, **135**, 1030–1043, doi:10.1002/qj.419.

——, M. J. Jarvis, L. J. Gray, and M. P. Baldwin, 2011: High- and low-frequency 11-year solar cycle signatures in the Southern Hemispheric winter and spring. *Quart. J. Roy. Meteor. Soc.*, **137**, 1641–1656, doi:10.1002/qj.852.

——, T. J. Bracegirdle, T. Phillips, and J. Turner, 2015: A comparative study of wave forcing derived from the ERA-40 and ERA-Interim reanalysis datasets. *J. Climate*, **28**, 2291–2311, doi:10.1175/JCLI-D-14-00356.1.

——, A. A. Scaife, G. J. Marshall, J. Turner, and L. J. Gray, 2017: Downward wave reflection as a mechanism for the stratosphere–troposphere response to the 11-yr solar cycle. *J. Climate*, **30**, 2395–2414, doi:10.1175/JCLI-D-16-0400.1.

Marchand, M., and Coauthors, 2012: Dynamical amplification of the stratospheric response simulated with the chemistry-climate model LMDz-Reprobus. *J. Atmos. Sol.-Terr. Phys.*, **75–76**, 147–160, doi:10.1016/j.jastp.2011.11.008.

Martineau, P., S.-W. Son, and M. Taguchi, 2016: Dynamical consistency of reanalysis datasets in the extratropical stratosphere. *J. Climate*, **29**, 3057–3074, doi:10.1175/JCLI-D-15-0469.1.

Matsuno, T., 1970: Vertical propagation of stationary planetary waves in the winter Northern Hemisphere. *J. Atmos. Sci.*, **27**, 871–883, doi:10.1175/1520-0469(1970)027<0871:VPOSPW>2.0.CO;2.

——, 1971: A dynamical model of the stratospheric sudden warming. *J. Atmos. Sci.*, **28**, 1479–1494, doi:10.1175/1520-0469(1971)028<1479:ADMOTS>2.0.CO;2.

McIntyre, M., 1982: How well do we understand the dynamics of stratospheric warmings? *J. Meteor. Soc. Japan*, **60**, 37–65, doi:10.2151/jmsj1965.60.1_37.

——, and T. N. Palmer, 1983: Breaking planetary waves in the stratosphere. *Nature*, **305**, 593–594, doi:10.1038/305593a0.

Mitchell, D. M., and Coauthors, 2015a: Signatures of naturally induced variability in the atmosphere using multiple reanalysis datasets. *Quart. J. Roy. Meteor. Soc.*, **141**, 2011–2031, doi:10.1002/qj.2492.

——, and Coauthors, 2015b: Solar signals in CMIP-5 simulations: The stratospheric pathway. *Quart. J. Roy. Meteor. Soc.*, **141**, 2390–2403, doi:10.1002/qj.2530.

Plumb, R. A., 1981: Instability of the distorted polar night vortex: A theory of stratospheric warmings. *J. Atmos. Sci.*, **38**, 2514–2531, doi:10.1175/1520-0469(1981)038<2514:IOTDPN>2.0.CO;2.

——, 2010: Planetary waves and the extratropical winter stratosphere. *Dynamics, Transport and Chemistry: A Festschrift to Celebrate Alan Plumb's 60th Birthday*, L. Polvani and A. Sobel, Eds., Amer. Geophys. Union, 23–42.

Polvani, L. M., and R. R. Saravanan, 2000: The three-dimensional structure of breaking Rossby waves in the polar wintertime stratosphere. *J. Atmos. Sci.*, **57**, 3663–3685, doi:10.1175/1520-0469(2000)057<3663:TTDSOB>2.0.CO;2.

Remsberg, E. E., 2014: Decadal-scale responses in middle and upper stratospheric ozone from SAGE II version 7 data. *Atmos. Chem. Phys.*, **14**, 1039–1053, doi:10.5194/acp-14-1039-2014.

Salby, M. L., 1984: Survey of planetary-scale traveling waves: The state of theory and observations. *Rev. Geophys.*, **22**, 209–236, doi:10.1029/RG022i002p00209.

Seppälä, A., H. Lu, M. A. Clilverd, and C. J. Rodger, 2013: Geomagnetic activity signatures in wintertime stratosphere wind, temperature, and wave response. *J. Geophys. Res. Atmos.*, **118**, 2169–2183, doi:10.1002/jgrd.50236.

Stewartson, K., 1977: The evolution of the critical layer of a Rossby wave. *Geophys. Astrophys. Fluid Dyn.*, **9**, 185–200, doi:10.1080/03091927708242326.

Tung, K. K., 1979: A theory of stationary long waves. Part III: Quasi-normal modes in a singular waveguide. *Mon. Wea. Rev.*, **107**, 751–774, doi:10.1175/1520-0493(1979)107<0751:ATOSLW>2.0.CO;2.

——, and R. S. Lindzen, 1979a: A theory of stationary long waves. Part I: A simple theory of blocking. *Mon. Wea. Rev.*, **107**, 714–734, doi:10.1175/1520-0493(1979)107<0714:ATOSLW>2.0.CO;2.

——, and ——, 1979b: A theory of stationary long waves. Part II: Resonant Rossby waves in the presence of realistic vertical shears. *Mon. Wea. Rev.*, **107**, 735–750, doi:10.1175/1520-0493(1979)107<0735:ATOSLW>2.0.CO;2.

Viereck, R. A., and L. C. Puga, 1999: The NOAA Mg II core-to-wing solar index: Construction of a 20-year time series of chromospheric variability from multiple satellites. *J. Geophys. Res.*, **104**, 9995–10 005, doi:10.1029/1998JA900163.

Walker, C. C., and G. Magnusdottir, 2003: Nonlinear planetary wave reflection in an atmospheric GCM. *J. Atmos. Sci.*, **60**, 279–286, doi:10.1175/1520-0469(2003)060<0279:NPWRIA>2.0.CO;2.

Waugh, D. W., and D. G. Dritschel, 1999: The dependence of Rossby wave breaking on the vertical structure of the polar vortex. *J. Atmos. Sci.*, **56**, 2359–2375, doi:10.1175/1520-0469(1999)056<2359:TDORWB>2.0.CO;2.

White, I. P., H. Lu, N. J. Mitchell, and T. Phillips, 2015: Dynamical response to the QBO in the northern winter stratosphere: Signatures in wave forcing and eddy fluxes of potential vorticity. *J. Atmos. Sci.*, **72**, 4487–4507, doi:10.1175/JAS-D-14-0358.1.

——, ——, and ——, 2016: Seasonal evolution of the QBO-induced wave forcing and circulation anomalies in the northern winter stratosphere. *J. Geophys. Res. Atmos.*, **121**, 10 411–10 431, doi:10.1002/2015JD024507.

Yamashita, Y., H. Akiyoshi, T. G. Shepherd, and M. Takahashi, 2015: The combined influences of westerly phase of the quasi-biennial oscillation and 11-year solar maximum conditions on the Northern Hemisphere extratropical winter circulation. *J. Meteor. Soc. Japan*, **93**, 629–644, doi:10.2151/jmsj.2015-054.